Non-canonical apical constriction shapes emergent matrices in *C. elegans*

Sophie S. Katz, Chloe Maybrun and Alison R. Frand*

Department of Biological Chemistry
David Geffen School of Medicine
University of California, Los Angeles
Los Angeles, CA 90095

*To whom correspondence should be addressed: afrand@mednet.ucla.edu

Keywords: Actomyosin cytoskeleton, adherens junctions, epidermal morphogenesis, cuticle patterning, *C. elegans* molting cycle

ABSTRACT

Specialized epithelia produce apical matrices with distinctive topographies by enigmatic mechanisms. Here, we describe a holistic mechanism that integrates cortical actomyosin dynamics with apical matrix remodeling to pattern *C. elegans* cuticles. Therein, axial AFBs appear near the surface of lateral epidermal syncytia during a pulse of transverse apical constriction (AC). AC generates temporary protrusions from the apical surface of epidermal syncytia, protrusions, coupled to a provisional matrix (sheath). In turn, sheath components pattern permanent ridges on the midline of adult cuticles (alae). Thus, forces generated by short-lived actin networks are relayed via the larval sheath to sculpt long-lived features of an acellular apical ECM. Further, we find that transient circumferential actin filament bundles (CFBs) in adjacent syncytia (hyp7) are largely dispensable for propagation of the annular cuticle features across development. Rather, these CFBs extend from actin bundles overlying body wall muscles and situated between known cell-ECM attachment complexes. Similar molecular and biophysical mechanisms may affect outcomes of AC and the formation of integumentary organs in higher metazoans.

INTRODUCTION

Polarized epithelial cells give rise to myriad architecturally distinct organs and appendages with specialized functions. These structures either include or adjoin apical extracellular matrices (aECMs) in contact with the environment. Examples in humans include stereocilia on auditory hair cells and microvilli on kidney and intestinal epithelia, which are projections from live cells embedded in matrices; hair, which is an amalgam of keratinized cells and extracellular molecules; and tooth enamel, which is an acellular, mineralized matrix. Mutations that affect related matrix proteins cause deafness, polycystic kidney disease and abnormal teeth (Devuyst et al., 2017; Legan et al., 2005; Masuya et al., 2005; Muller and Barr-Gillespie, 2015). Moreover, carcinomas co-opt physiologic mechanisms that regulate the turnover of apical matrices (Braidotti et al., 2004; Jonckheere et al., 2010). Despite the medical significance of the integument, the cell and molecular mechanisms that sculpt apical matrices are not well understood.

Development of many epithelial tissues involves selective constriction of the apical surface of one or more cells (Heer and Martin, 2017; Iruela-Arispe and Beitel, 2013). Resulting changes in cell shape promote morphogenetic processes ranging from gastrulation to formation of bronchial buds and branches (Kim et al., 2013; Martin et al., 2010; Vasquez et al., 2014). The mechanical networks that drive apical constriction (AC) include actomyosin filaments and/or bundles that generate contractile forces; cell-cell junctions that link actomyosin filaments in adjacent cells; and cortical flows, which promote assembly of actin filaments at regions under tension (Hannezo et al., 2015). Fine spatial and temporal regulation of actomyosin contractility achieves the correct, contextual shape changes. Although these mechanical networks are well characterized (Martin and Goldstein, 2014), the extent to which they shape apical matrices is unclear. Conversely, the contributions of apical matrices to tissue-level outcomes of AC remain enigmatic. This gap reflects our relatively limited knowledge about biochemical and biophysical properties of apical ECMs, as compared with basement membranes.

The key cell and molecular components driving apical constriction are conserved between nematodes and mammals. As depicted in Figure 1, the epidermis of *C. elegans* consists mainly of the lateral stem cell-like seam cells and the adjacent hyp7 syncytium. The seam cells undergo asymmetric division early in each larval stage. The posterior daughters remain in the seam while the anterior daughters fuse with hyp7. During the larval-to-adult transition, seam cells undergo homotypic fusion, becoming bilateral syncytia, and enter persistent cell-cycle quiescence (Sulston and Horvitz, 1977). By then, the hyp7 syncytium includes 139 nuclei (Yochem et al., 1998). Hyp7 has four discernable sub-regions: thick bilateral regions; dorsal and ventral ridges; and thin segments anchored to underlying body wall muscles by trans-epidermal attachments called fibrous organelles (Bosher et al., 2003). Together, the seam and hyp7 synthesize most of the body cuticle.

92 The apical-lateral junctions among epithelial cells of *C. elegans* are analogous to those found
93 in vertebrates and insects (Pasti and Labouesse, 2014). Homologs of α-catenin, ß-catenin, p120-
94 catenin, and e-cadherin, all of which are components of mammalian adherens junctions (AJs),
95 form a complex subjacent to the apical membrane (Costa et al., 1998; Loveless and Hardin,
96 2012). The worm homolog of the *Drosophila* septate junction component Discs-large and the
97 nematode-specific protein AJM-1 comprise a distinct basal complex (Koppen et al., 2001;
98 McMahon et al., 2001).
99 The *C. elegans* cuticle is an acellular, multi-layered extracellular matrix mainly composed of
100 collagens (Page and Johnstone, 2007), rather than the polysaccharide chitin found in insects
101 (Fabritius et al., 2011). The first cuticle is produced late in embryogenesis beneath a provisional
102 matrix called the embryonic sheath (Priess and Hirsh, 1986). Each larval-stage cuticle is shed
103 and replaced with a larger structure during the subsequent four molts (Knight et al., 2002; Sulston
104 and Horvitz, 1977). The adult-stage cuticle lasts for weeks, rather than hours, as adults no longer
105 molt.
106 The prevailing model for the process of molting includes three sequential steps: 1) detachment
107 of the epidermis from the preexisting cuticle (apolysis); 2) synthesis of the new cuticle directly
108 beneath the old; and 3) escape from the old cuticle (ecdysis) (Jenkin and Hinton, 1966; Locke
109 and Huie, 1979; Truman, 1992). Because this model does not invoke a provisional enclosure, it
110 cannot explain how squishy nematodes remain intact, rather than implode. We recently learned
111 that *C. elegans* larvae produce an interim aECM (sheath) between the epidermis and the old
112 cuticle as they begin to molt (Fig. 1). Notably, specific components of the sheath are patterned
113 like the upcoming, rather than passing, cuticle. The sheath and old cuticle are shed together at
114 ecdysis ((Katz et al., 2015), with permission).
115 Three longitudinal ridges (alae) overlying the syncytial seam are prominent features of the
116 adult-stage cuticle. Because the alae arise above the syncytial seam during the larval-to-adult
117 transition, numerous studies vis-à-vis the succession of temporal cell fates have scored alae
118 formation as a proxy for maturation of the epidermis (Ambros and Horvitz, 1984). Similarly
119 positioned but morphologically distinct alae are found on the cuticles of L1s and dauers, which
120 are stress-induced variants of L3s (Hu, 2007); but not on the cuticles of L2s, L3s or L4s. To our
121 knowledge, the role of actomyosin-based mechanical networks in patterning the alae has not
122 previously been examined. Indeed, the cortical actin networks of larval seam cells and syncytia
123 have not been described.
124 Scores of evenly-spaced circumferential bands (annuli) separated by narrow furrows are also
125 found in the outermost layers of all 5 stage-specific cuticles, overlying hyp7 and other epithelia
126 (Page and Johnstone, 2007). The spacing of the annuli is thought to be similar in larvae and
127 young adults (Cox et al., 1981b). More recent studies of adult animals carrying mutations that
128 affect body morphology have shown that the frequency of annuli along the long axis of the body

129 scales with size (Essmann et al., 2017). Parallel rows of circumferentially-oriented cortical actin
130 filament bundles (CFBs) assemble and disassemble in the hypodermis while embryos elongate
131 and again while larvae molt. The CFBs of embryos are thought to pattern the annuli of L1-stage
132 cuticles (Costa et al., 1997; Priess and Hirsh, 1986). However, the mechanism that subsequently
133 relays this annular pattern from effete to emergent cuticles is not known.

134 Here, we describe a novel and potentially conserved morphogenetic mechanism that
135 integrates cortical actin dynamics with apical matrix remodeling. Therein, a pulse of anisotropic
136 apical constriction generates temporary protrusions from epithelia coupled to the provisional
137 sheath, which then patterns durable ridges (alae) on *C. elegans* cuticles. In this non-canonical
138 system, interim matrices serve as key components of mechanical networks that shape
139 integumentary appendages. In addition, we provide evidence that transient CFBs present in the
140 hypodermis of molting animals appear to be elaborations of continual but previously unrecognized
141 cortical actin bundles overlying body wall muscles, rather than form factors for the annuli.

142

143 **RESULTS**

144 **Actin and NMYII pattern longitudinal, rather than annular, folds in adult cuticles.**

145 To evaluate the role of actin filaments and/or bundles in patterning emergent cuticles, we used
146 both bacterial-mediated RNA-interference (RNAi) and conditional mutations to knockdown actin
147 and non-muscle myosin II (NMYII) while larvae developed and then examined the lateral surface
148 of young adults. Longitudinal ridges overlying seam syncytia (alae) were directly observed by DIC
149 microscopy. Raised circumferential bands overlying hyp7 (annuli) were detected by staining
150 animals with the fluorescent lipophilic dye DiI prior to observation (Schultz and Gumienny, 2012).

151 Five genes of *C. elegans* encode actin. Epidermal cells and syncytia express *act-1, -2*, *-3* and
152 possibly *-4* but evidently not *act-5* (MacQueen et al., 2005; Sarov et al., 2012; Willis et al., 2006).
153 To simultaneously knockdown *act-1*, *-2*, *-3* and *-4*, we selected a dsRNA trigger complementary
154 to all four transcripts. Further, we customized and applied an established experimental paradigm
155 to selectively knockdown *actin* in the seam or hyp7. This system entails the tissue-specific
156 expression of wild-type *rde-1*, which encodes the worm homolog of Argonaute, in *rde-1(null)*
157 mutants otherwise insensitive to siRNAs (Qadota et al., 2007; Steiner et al., 2009). Epidermis-
158 specific knockdown of *actin* minimized the larval lethality associated with systemic RNAi of *actin*
159 over the 42-hour course of larval development. Attenuated exposure to *actin* dsRNAs for only 30
160 hours starting in the L2 stage also bypassed this lethality, allowing otherwise wild-type,
161 *actin(RNAi)* larvae to develop into relatively small adults.

162 Preferential knockdown of *actin* in either the seam or hyp7 led to the formation of grossly
163 misshapen patches of cuticle, which interrupted the three ridges characteristic of adult-stage alae
164 (Fig. 2A). Patches with many tortuous, short ridges and discontinuous longitudinal ridges were
165 observed on 93% of seam-specific *actin(RNAi)* animals and 89% of hyp7-specific *actin(RNAi)*

166 animals (n≥100). Hereafter, we refer to such patches as “mazes.” The most extensive mazes
167 lacked detectable dorsal and ventral ridges. Such deformities were not found on the lateral
168 surface of *rde-1(null)* mutants fed the same bacteria transformed with empty vector. However,
169 mazes were observed on 89% of wild-type animals following attenuated exposure to *actin*
170 dsRNAs (Fig. 2A-B). Some mazes appeared next to large (>5μm) stretches of cuticle devoid of
171 longitudinal ridges. These stretches uniformly aligned with gaps in the subjacent seam syncytium
172 detected by DIC and fluorescence microscopy. These gaps may be attributable to the loss of
173 seam nuclei during aberrant, larval-stage cell divisions. Accordingly, in our scoring rubric mazes
174 were prioritized *post-hoc*, over large gaps and minor deformities found along the midline of any
175 particular worm.

176 Two genes of *C. elegans* encode NMYII heavy chains approximately 47% identical to human
177 NMMHC-IIB, and active in the epidermis (Piekny et al., 2003). We used *nmy-1(RNAi)* and
178 conditional *nmy-2(ts)* alleles to partially inactivate NMYII throughout this study. Mazes, by and
179 large extensive, were observed on 94% of *nmy-1(RNAi); nmy-2(ne3409ts)* double mutants and
180 97% of *nmy-1(RNAi); nmy-2(ne1490ts)* double mutants raised at restrictive temperature (Fig. 2A-
181 B). Minor deformities in the alae such as small divots were observed on 82% of *nmy-1(RNAi)*
182 single knockdowns and a minority of *nmy-2(ne3409ts)* and *nmy-2(ne1490ts)* single mutants.
183 Collectively, these findings suggest that actomyosin networks within the seam and hyp7 syncytia
184 cooperatively shape the adult-stage alae. The *nmy-1* and -2 genes may act redundantly or
185 cooperatively in this context.

186 As described, DiI labels raised segments of the cuticle including alae and annuli but does not
187 impregnate adjacent valleys and furrows (Schultz and Gumienny, 2012). As expected, DiI stained
188 scores of evenly-spaced circumferential annuli on dorsolateral and ventrolateral surfaces of wild-
189 type adults (Fig. 2C). DiI also labeled evenly-spaced, annular bands on the surface of *actin(RNAi)*
190 adults, while labeling mazes on the lateral midline. The average spacing of furrows *actin(RNAi)*
191 animals was 1.3μm±0.2 (mean and SD), compared to 1.7μm±0.4 in age-matched controls. This
192 was consistent with the small size of *actin(RNAi)* adults and the reported scaling of these two
193 morphometric features (Essmann et al., 2017). DiI likewise stained evenly-spaced, annular bands
194 on the surfaces of *nmy-1(RNAi)* single knockdowns, *nmy-2(ts)* single mutants, and *nmy-1(RNAi)*
195 *nmy-2(ts)* double mutants, which had grossly misshapen alae (Fig. 2C). Because DiI consistently
196 saturated the alae, signal in adjacent regions of the cuticle often appeared less intense and more
197 variable among isogenic worms. The formal possibility that these knockdowns lead to subtle
198 defects in the curvature or texture of annuli cannot be eliminated using this approach.
199 Nonetheless, we found no evidence that regenerating the pattern of annuli in adult cuticles
200 requires actin or NMYII, whereas *de novo* patterning of the alae clearly required the corresponding
201 genes. This particular finding contradicts the widely-accepted model that transient CFBs present
202 in hyp7 during molts pattern the annuli of nascent cuticles (Costa et al., 1997).

203

204 **AJ components that interact with actin networks shape the adult-stage alae.**

205 To evaluate the role of cell-cell junctions in patterning emergent cuticles, we similarly used
206 RNAi and a hypomorphic allele to knockdown key AJ components while larvae developed and
207 then examined the lateral surface of young adults. As described, HMP-1/α-catenin is the actin-
208 binding component of cadherin-catenin complexes (CCCs) that mechanically link the various
209 epidermal cells of *C. elegans* (Costa et al., 1998; Kang et al., 2017; Loveless and Hardin, 2012).
210 The Zonula Occludens (ZO) homolog ZOO-1 cooperatively recruits actin bundles to AJs
211 (Lockwood et al., 2008). We used the substitution mutation *hmp-1(fe4)* because the
212 corresponding protein has decreased affinity for actin but approximately half of the homozygous
213 mutants complete embryonic and larval development (Maiden et al., 2013; Pettitt et al., 2003).
214 We used RNAi of *zoo-1* to sensitize the genetic background. Mazes were observed on the surface
215 of 46% (n=107) of *zoo-1(RNAi); hmp-1(fe4)* double mutants (Fig. 3A-B). Continuous dorsal and
216 ventral ridges framed the majority of these mazes, as observed upon attenuated RNAi of *actin* in
217 wild-type adults (Fig. 2A). Further reduction of *hmp-1* activity may well result in extensive mazes.
218 DiI labeled periodic, annular bands on the dorsolateral and ventrolateral surfaces of all (n=17)
219 *zoo-1(RNAi; hmp-1(fe4)* double mutants, despite the high penetrance of misshapen alae (Fig.
220 3C). Furrow spacing in the double mutants was 1.4μm±0.4 compared to 1.7μm±0.4 in age-
221 matched wild type controls, consistent with the smaller size characteristic of *hmp-1(fe4)* mutants.
222 The DiI signal and background fluorescence appeared more intense on *hmp-1(fe4)* mutants than
223 wild type adults. This difference may result from relatively inefficient removal of unbound dye
224 through free movement on NGM plates, as the locomotion of *hmp-1(fe4)* adults was visibly
225 impaired. Thus, genetic manipulations that compromise the ability of AJs to transmit forces
226 between the seam and hyp7 abrogated the pattern of adult-stage alae but had little, if any, effect
227 on propagation of the pattern of annuli from L1- to adult-stage cuticles.

228

229 **Cortical actin dynamics linked to pulsatile apical constriction of seam syncytia**

230 To further investigate the role of actin networks and AJs in shaping emergent alae, we tracked
231 the distribution of F-actin at the cortex of seam cells and syncytia in animals developing from the
232 L3 to the adult stage (Fig. S1, Fig. 4). For this purpose, we constructed a genetically-encoded
233 sensor for F-actin comprising the Calponin homology domain (CH) of human Utrophin (UTRN)
234 tagged with GFP and driven by the seam-specific promoter of *elt-5* (Koh and Rothman, 2001).
235 This approach enabled highly-sensitive live-imaging because UTRNCH::GFP binds F-actin
236 selectively and reversibly; in addition, UTRNCH::GFP has no appreciable effect on actin
237 rearrangements when expressed at practical levels (Burkel et al., 2007; Moores and Kendrick-
238 Jones, 2000). To capture both cell and molecular dynamics germane to morphogenesis of the
239 alae, we combined AJM-1::mCHERRY, an established marker for adherens junctions (Koppen et

240 al., 2001), with the seam>UTRNCH::GFP sensor. To achieve fine temporal resolution, we isolated
241 precisely staged transgenic nematodes as follows: We selected ~60 individuals transiting the
242 L3/L4 molt from synchronously developing populations and watched them; the time when a given
243 worm emerged in L4 was set to zero; we then collected cohorts of ~7 worms at regular ~1hr
244 intervals and imaged both GFP and mCherry near the apical surface of the lateral epidermis using
245 confocal fluorescence microscopy.

246 As described, homotypic fusion follows the last round of asymmetric division and precedes
247 the onset of the final (L4/A) molt (Podbilewicz and White, 1994) (Fig. 4A). The seam syncytia go
248 on to make the adult-stage alae during the molt. As shown in Fig. S1, the rectangular seam cells
249 of late L3 larvae were connected to each other and hyp7 by AJs incorporating AJM-1::mCHERRY.
250 UTRNCH::GFP labeled F-actin within cortical meshworks and alongside AJs. The seam cells
251 became more ellipsoidal during the L3/L4 molt and divided shortly thereafter. The anterior
252 daughters fused with hyp7 as the posterior daughters reconnected (Fig. S1). Surprisingly, we
253 found seam syncytia, rather than individual cells, in all nematodes imaged 3-hours after
254 emergence in L4 (Fig. 4B). Capturing the dynamic redistribution of cortical actin during
255 asymmetric division, cytokinesis, migration of the posterior daughters and homotypic fusion of the
256 seam cells validated our key reagents and approach.

257 Straightaway, the apical surface of seam syncytia narrowed, as AJs demarcating the dorsal
258 and ventral margins drew closer together (Fig. 4B, 3hrs). The apical surface of the seam then
259 widened slowly, as the AJs spread apart over the following 4-5hrs. This interval included much of
260 the L4/adult molt (Fig. 4B, molt). The observed shape changes indicated a pulse of anisotropic
261 constriction on the D-V (transverse) axis followed by gradual relaxation. Indeed, at the apex of
262 constriction 4hrs into the L4 stage, the width of the seam was 1.9μm ±0.3μm (mean and SD),
263 compared to 3.2μm ±0.7μm before constriction (3hrs in L4) and 2.8μm ±0.4μm at 6hrs in L4. As
264 described below, concurrent changes in the ultrastructure of the epidermis detected by
265 transmission electron microscopy (TEM) further substantiated this model (see Fig. 6).

266 Two longitudinal actin bundles rapidly assembled at the cortex of seam syncytia, co-localizing
267 with AJs along the dorsal and ventral margins (Fig. 4B, arrows). These particular actin bundles
268 persisted as the seam narrowed. The extent to which longitudinal actin bundles overlapped with
269 AJs diminished as the seam widened. Instead, we detected spikes of F-actin orthogonal to the
270 margins (Fig. 4B, chevrons). These spikes increased in size but decreased in number as larvae
271 entered the molt and emerged as young adults. This dramatic reorientation of marginal F-actin
272 relative to AJs suggested a corresponding change in the routing of forces between the seam and
273 hyp7.

274 Two more actin bundles assembled in the middle of seam syncytia (Fig. 4B, dashes). These
275 medial-axial bundles moved closer together as the seam narrowed, spread apart as the seam
276 widened, and endured the process of molting. Cortical meshworks were detected at all times but

277 relatively difficult to discern in narrow syncytia. At the apex of apical constriction, the pattern of
278 longitudinal actin cables near the surface of seam syncytia bore a striking resemblance to the
279 adult-stage alae, manifest ~6hrs later. To summarize, we detected four longitudinal actin bundles
280 at 3hrs in L4, prior to seam constriction. At the apex of constriction (4hrs in L4), we detected three
281 longitudinal actin bundles. As the seam widened again, two medial-axial bundles persisted,
282 whereas F-actin spikes appeared at the junctions.
283 To identify cortical actin structures that most likely generate or route mechanical forces
284 relevant to patterning the alae, we considered that tension *per se* stabilizes actomyosin filaments
285 and related adhesive complexes (Borghi et al., 2012; Hannezo et al., 2015; Wu and Yap, 2013).
286 For this reason, we examined the distribution of AJs and cortical actin in NMYII knockdowns
287 transiting the L4/A molt (Fig. 5). AJs demarcating the dorsal and ventral margins of seam syncytia
288 were tortuous but typically farther apart in *nmy-1(RNAi); nmy-2(ne3409ts)* double mutants than
289 age-matched transgenic nematodes. Distension of the seam syncytia seemed to account for the
290 girth of cuticular mazes found on *nmy-1(RNAi); nmy-2(ts)* adults (Fig. 2A). Further, medial-axial
291 actin bundles and cohesive cortical meshworks were not detected in the seam syncytia of
292 *nmy-1(RNAi); nmy-2(ne3409ts)* double mutants, but were found in control specimens (Fig. 5,
293 dashes). Distended seam syncytia lacking medial-axial actin bundles and cohesive cortical
294 meshworks were likewise observed in *nmy-1(RNAi); nmy-2(ne1409ts)* double mutants.
295 Qualitatively similar but less severe abnormalities were observed in the corresponding single
296 mutants (Fig. 5). In contrast, spikes of F-actin orthogonal to AJs were readily detected in *nmy-1*
297 *nmy-2* double and single knockdowns, as well as control specimens. Thus, the assembly and/or
298 persistence of medial actin cables and meshworks near the apical surface of seam syncytia
299 depends on NMYII more than the assembly and/or persistence of peripheral spikes. Taken
300 together, these findings suggest that cortical tension contributes to apical constriction of the seam
301 syncytia, its measured relaxation and/or maintenance of the resulting shape of seam syncytia,
302 which are distinct but likely interdependent processes.
303
304 **Tension-dependent recruitment of F-actin to the margins of hyp7**
305 As our initial findings indicated that actomyosin networks in both the seam and hyp7 syncytia
306 contribute to morphogenesis of the alae, we went on to track the distribution of cortical actin in
307 hyp7 across the larval-to-adult transition (Fig. 6, Fig. S2). For this purpose, we constructed a
308 similar but distinct F-actin sensor comprising UTRNCH tagged with dsRED and driven by the
309 hypodermal-specific minimal promoter of the cuticle collage gene *dpy-7* (Johnstone et al., 1992).
310 Longitudinal actin bundles were detected along the lateral margins of hyp7 throughout L4 and the
311 L4/A molt (Fig. 6A & B). The intensity of corresponding signals peaked ~6hrs after larvae emerged
312 in the L4 stage and plummeted as adults escaped from the larval cuticle. Spikes of F-actin
313 orthogonal to the lateral margins were also detected in molting animals. To evaluate the possibility

314 that actin at the margins of hyp7 regulates changes in seam cell shape, we examined these
315 structures after genetic inactivation of NMYII. Signals from hyp7>UTRNCH::dsRED were barely
316 detectable at the boundary between hyp7 and seam syncytia in *nmy-1(RNAi); nmy-2(ne3409)*
317 double mutants molting from L4 to the adult stage (Fig. 6D). The average fluorescence intensity
318 at this boundary was 72±22 a.u. (N=5) in double mutants, compared to 116±20 a.u. (N=7) in
319 transgenic but otherwise wild type animals (Fig. 6E). Finding that actomyosin contractility
320 maintains actin bundles on the hyp7 side of AJs suggests that these force-transmitting complexes
321 regulate the pulse of apical constriction of the seam syncytia during the larval-to-adult transition.
322 Cortical meshworks were detected in the lateral (thick) regions of hyp7 syncytia ~3hrs after
323 larvae emerged in the L4 stage. Parallel arrays of circumferentially-oriented actin filament bundles
324 (CFBs) assembled near the apical surface of hyp7 over the following 3hrs; persisted through the
325 molt; and then abruptly collapsed. These dynamics were substantiated by anisotropy values (a
326 metric for parallel alignment) of UTRNCH::dsRED signals in this region of interest. On average,
327 anisotropy values increased 5-fold during the L4 stage, remained high for most of the L4/A molt,
328 plummeted at ecdysis, and returned to base-line in young adults (Fig. 6C). We further examined
329 the status of CFBs in hyp7 upon inactivation of NMYII. CFBs persisted in virtually all
330 *nmy-1(RNAi); nmy-2(ne3409)* double mutants and corresponding single mutants molting from L4
331 to adult (Fig. 6D). In one double mutant, neither the seam syncytium nor CFBs were detected,
332 indicating an atypically severe phenotype. Consistent with these observations, no significant
333 differences were found among mean anisotropy values for UTRNCH::dsRED in mutants versus
334 control (Fig. 6F). Thus, neither the assembly or maintenance of CFBs in lateral regions of hyp7
335 was obviously dependent on actomyosin contractility. Moreover, the increased variability in
336 anisotropy values associated with NMYII knockdown was not mirrored by irregular patterning of
337 the annuli (Fig. 2C). As such, it is unlikely that CFBs directly pattern the annuli or propagate their
338 pattern from L4 to adult-stage cuticles. The kinetics of CFB assembly and disassembly further
339 suggested an alternative function.
340
341 **Transient CFBs in lateral hyp7 connect to stable CFBs in hyp7 over muscle.**
342 During the above-mentioned study, we noticed that some of the transient CFBs detected in
343 the lateral region of hyp7 across the L4-to-adult transition extended into the quadrant of hyp7
344 overlying body wall muscle (Fig. 6D and Fig. S2). These previously unrecognized CFBs in hyp7
345 overlying body wall muscle (mCFBs) were consistently observed in L4, molting animals, and
346 adults (Fig. S2A and B). The mCFBs were situated between *Ce.* hemidesmosomes (*Ce*HDs) (Fig.
347 S2B and C) labeled either by MUP-4::GFP, which is an affiliated apical ECM receptor (Hong et
348 al., 2001) or VAB-10A::GFP, which is the core *Ce*HD spectraplakin (Morrissey et al., 2014). These
349 findings suggest that mCFBs are components of stable attachment complexes distinct from
350 *Ce*HDs.

351

352 **Ultrastructure of the epidermis during deposition of the alae.**

353 Rapid constriction and slow expansion of seam syncytia regulated by actomyosin networks
354 hinted at reversible folding of the apical surface over the larval-to-adult transition. We therefore
355 used transmission electron microscopy to further characterize related changes in the
356 ultrastructure of the lateral epidermis and overlying matrices.

357 The TEM micrographs in Figure 7 show transverse sections through the lateral epidermis of
358 early versus mid L4 larvae presented in initial studies of the molting cycle and reproduced with
359 permission (Singh and Sulston, 1978). The apical surface of the seam narrowed midway through
360 L4. The width of the seam decreased by approximately 3.5-fold as indicated by the distance
361 between the two apical-lateral junctions with hyp7. Three discrete protrusions (blebs) were
362 detected on the apical surface. Two blebs were situated above seam-hyp7 junctions, and one
363 near the middle of the seam syncytium. A thin but continuous ECM was detected above the
364 epidermis and beneath the preexisting larval cuticle, covering all three cellular protrusions. This
365 distinctive apical matrix almost certainly corresponds to the molting sheath recognized some
366 40yrs later (Katz et al., 2015).

367 Inward deformation and gradual expansion of the apical membrane of the seam syncytium
368 followed during the L4-to-adult molt, producing a large pocket in which the alae were deposited
369 (Fig. 7B). As the seam widened, the seam-hyp7 junctions moved farther away from the nascent
370 alae, whose position on the D-V axis did not change appreciably across the molt. Progressive
371 deposition of the alae beneath the L4 cuticle and remnants of the sheath were indicated by the
372 increasing height of the ECM ridges. Secretory granules were present within the seam syncytium,
373 below the growing alae and intervening segments of the apical membrane. Notably, the L4 cuticle
374 thinned as the alae grew, suggesting that the effete cuticle was partially dismantled and possibly
375 recycled. In young adults, the surface of the lateral epidermis followed the contour of the body
376 and the ridges of the tripartite alae were apparent (Fig. 7C).

377

378 **Provisional sheaths relay cortical actin dynamics to fixed patterns in apical matrices.**

379 Based on the spatial and temporal correlations among the longitudinal actin bundles present
380 in seam syncytia at the apex of constriction (Fig. 4B); transient protrusions from the apical surface
381 of seam syncytia (Fig. 7A); and the appearance of longitudinal bands in the provisional sheaths
382 of animals molting from L4 to the adult stage (Fig. 8), we hypothesized that cortical actin dynamics
383 were mechanically coupled to this short-lived aECM. As an initial test of this hypothesis, we
384 determined the effect of attenuated *actin* RNAi on the pattern of two components of the L4/A
385 sheath; namely, the ZP-domain proteins FBN-1 and NOAH-1. Both *fbn-1* and *noah-1* emerged
386 from a preliminary, RNAi-based screen for knockdowns unable to molt (Frand et al., 2005).
387 Thereafter, we constructed full-length (FL) *fbn-1::mcherry* and *noah-1*::*sfgfp* translational fusion

genes within distinct extrachromosomal arrays (*aaaEx78* and *aaaEx167*). These arrays rescued the lethality caused by respective null alleles of *fbn-1* or *noah-1*, confirming the production of functional fusion proteins. As previously described and shown in Fig. 8A, circumferential bands of FL-FBN-1::mCHERRY corseted the body while larvae underwent molts and while embryos elongated. Longitudinal bands of FL-FBN-1::mCHERRY were also detected above the seam syncytia during the L4/A molt. The pattern of these bands presaged the forthcoming alae (Katz et al., 2015). Longitudinal and circumferential bands of NOAH-1::sfGFP were also detected above the seam syncytia during the L4/Adult molt (Fig. 8B). In this case, the fluorescent signal localized to four distinct stripes aligned with light-refractive regions of the nascent cuticle visible by DIC; these stripes likely correspond to temporary valleys flanking the emergent alae.

Following attenuated RNAi of *actin*, FL-FBN-1::mCHERRY localized to labyrinthine deformities, rather than longitudinal bands, overlying the lateral surfaces of emergent adult-stage cuticles (Fig. 8A). The abnormal pattern of FL-FBN-1::mCHERRY within the sheath matched the abnormal pattern at the surface of emergent cuticles detected by DIC. Attenuated RNAi of *actin* also led to the deposition of NOAH-1::sfGFP mazes perfectly aligned with misshapen valleys in the emergent cuticle above the seam syncytia (Fig. 8B). In contrast, the annular patterns of FL-FBN-1::mCHERRY and NOAH-1::sfGFP were superficially normal in *actin(RNAi)* animals, consistent with our initial findings that both epidermis-specific and systemic but attenuated RNAi of *actin* impaired *de novo* patterning of the alae, rather than propagation of the pattern of annuli.

The above-mentioned hypothesis further predicts that knocking-down certain sheath components will lead to deformities in apical ECMs. We therefore examined the lateral surfaces of young adults following attenuated but systemic RNAi of *noah-1.* Mazes and minor deformities in the alae were detected in 81% (N=100) of *noah-1(RNAi)* adults, but were not detected in same-day controls, consistent with our working model that provisional sheaths propagate cortical actin dynamics underlying transient changes in epithelial cell shape to sculpt more durable apical matrices.

Having conceived this working model and validated its key predictions in the context of the larval-to-adult transition, we asked whether a similar, if not identical, morphogenetic mechanism gives rise to the architecturally distinct alae of dauers. To address this question, we combined the conditional *daf-2(e1370)* allele, which confers a dauer-constitutive (Daf-c) phenotype at restrictive temperature, with our seam>UTRNCH::GFP sensor for F-actin and our FL-FBN-1::mCHERRY marker for the provisional sheaths of molting worms. We then imaged UTRNCH::GFP in live nematodes molting from L2d to dauer, a process that involves extreme radial constriction of the body. Early in the molting process, dense cortical meshworks including both longitudinal and transverse actin filaments and/or bundles were detected in rather wide, seam cells (Fig. S3A). Some of these structures appeared supracellular, crossing cell boundaries, or were aligned in adjacent cells. Later in the process, we detected spikes of actin orthogonal to junctions between

425 seam cells and hyp7 in the very thin seam cells of fully constricted animals. We also imaged
426 FL-FBN-1::mCHERRY across the L2d to dauer molt. The pattern of FL-FBN-1::mCHERRY in the
427 corresponding sheath included five longitudinal stripes within a wide lateral band (Fig. S3B). While
428 this pattern was markedly different from the sheaths of animals molting from L4 to the adult stage,
429 the pattern of FBN-1 stripes yet again presaged the shape of the forthcoming dauer-specific alae,
430 which have four ridges that span most of the lateral surface of the cuticle (Fig. S3C). In addition,
431 the lack of detectable FL-FBN-1::mCHERRY signal on the surface of dauers was consistent with
432 the temporary nature of the sheath, which was partly consumed and partly shed with the L2
433 cuticle. These observations are entirely consistent with temporal reiteration of a common
434 morphogenetic mechanism.
435
436 **DISCUSSION**

437 Figure 9 provides cohesive model for morphogenesis of the lateral epidermal syncytia and
438 cuticle of adult-stage *C. elegans*, based on key findings from descriptive and mechanistic studies.
439 Therein, rearrangements in cortical actin networks effect transitory changes in cell shape and
440 tissue architecture, which are relayed through the provisional sheath to pattern permanent ridges
441 on the cuticle. Midway through the 4th larval stage, the seam syncytium narrows rapidly on the
442 dorsal-ventral axis (Fig. 9A 1-2). Forces generated by actomyosin filaments and propagated
443 through adherens junctions evidently drive this change in shape, as knockdowns of epidermal
444 actin, NMYII, and HMP-1 all give rise to distended seam syncytia and/or mazes. Longitudinal actin
445 bundles assemble on both sides of seam-hyp7 junctions during this phase; as described below,
446 these parallel bundles may act cooperatively to drive AC. Next, the seam syncytium widens
447 slowly, suggesting the gradual release of cortical tension. Such relaxation is atypical among
448 morphogenetic processes dependent on AC, as molecular ratchets often fix the shapes of
449 constricted cells (Mason et al., 2013). Spikes of F-actin orthogonal to seam-hyp7 margins arose
450 during the relaxation phase. Related adhesive complexes may allow the seam to push back
451 against hyp7 (Fig. 9A 2-3) and so resemble dynamic endothelial junctions (Cao et al., 2017;
452 Lampugnani, 2010).

453 The forces that drive constriction of the seam syncytium also generate three cellular
454 protrusions via outward folding of the apical membrane: one above the dorsal junction with hyp7,
455 one in the middle of the seam syncytium, and one above the ventral junction (Fig. 9B, right).
456 These protrusions effectively mark the sites of forthcoming ridges in the adult cuticle. The outer
457 blebs spatially and temporally correspond with longitudinal actin bundles that co-localize with AJs.
458 The middle bleb probably forms above the medial-axial actin bundles, which persist well into the
459 molt. The blebs are another noteworthy aspect of this system, given that AC typically leads to
460 inward cellular deformations and tissue invagination (Heer and Martin, 2017), with few exceptions
461 such as budding of the lungs (Kim et al., 2013). However, F-actin has been detected in cellular

462 blebs during the formation of taenidial folds in the *Drosophila* trachea, as the chitinous aECM is
463 deposited {Ozturk-Colak, 2016 #121}.
464 As described, all three protrusions appear beneath the molting sheath, which is a temporary
465 extracorporeal enclosure composed of several ZP-domain proteins. Although the blebs are
466 ephemeral, the pattern of the lateral sheath mimics the cellular protrusions and the forthcoming
467 alae. In this context, the sheath relays forces from passing actin networks to shape upcoming
468 substructures in durable cuticles. This could occur through transient coupling of the actin
469 cytoskeleton to specific sheath components by a currently unknown transmembrane receptor.
470 Consistent with this model, attenuated knockdown of *actin* abrogates the pattern of longitudinal
471 cables within the sheath visualized by FBN-1 and NOAH-1 fusion proteins. In turn, knockdown
472 of *noah-1* gives rise to mazes, rather than continuous ridges (alae), on the cuticles of young
473 adults. This last finding identifies the sheath as a key intermediate in morphogenesis of the alae,
474 a process that begins with AC and overcomes delays linked to systemic tissue remodeling.
475 Three prospective properties would enable the sheath to transmit the pattern of cellular blebs
476 to the ridges of the alae: cell-aECM adhesion, mechanical resilience and space-filling. In theory,
477 adhesion between the cellular protrusions and the sheath could preserve their form while the
478 seam begins to relax. Potential receptors include MUP-4 and MUA-3, which are nematode-
479 specific apical ECM receptors associated with CeHDs (Bercher et al., 2001; Hong et al., 2001)
480 and the two dimeric integrins expressed by *C. elegans* (Cox and Hardin, 2004), which might
481 interact with the canonical integrin-binding motifs present in FBN-1. In this system, mechanical
482 forces generated by the actomyosin cytoskeleton in the underlying epidermis are routed through
483 the sheath. Related tension-bearing capacity could be provided by organization of ZP-domain
484 meshwork or resilience of specific components therein. Lastly, the sheath occupies space, filling
485 the pocket created by inward deformation of the seam membrane, consistent with O-linked
486 glycosylation of ZP-domain proteins (Gupta et al., 1999). The sheath is dismantled as the alae
487 are progressively secreted, and this may account for accretion of related fluorescent signals in
488 the valleys between and alongside ridges of the alae approaching ecdysis.
489 While we do not yet know the extent to which longitudinal actomyosin filament bundles (AFBs)
490 within the curved cortex of seam syncytia drive constriction on the transverse (D-V) axis, rather
491 than cortical meshworks; we recognize two applicable mechanisms. First, cross-linking of
492 longitudinal AFBs to one another and/or cortical meshworks would allow for transverse
493 propagation of contractile forces. Prospective cross-linkers include alpha-actinin and formin,
494 which regulate actin dynamics in other instances of AC (Mason et al., 2013). Second, the syncytial
495 seam can be modeled as a sealed cylinder with internal, pressurized fluids. As such, the predicted
496 effect of axial stress is buckling (continuous blebs) on the A-P axis (Nelson, 2016), and the
497 production of circumferential and transverse force vectors (Hayashi et al., 2018; Shih et al., 2017),
498 which may promote anisotropic constriction or bear tension to resist excessive expansion.

499 Modeling the seam syncytium in this way further suggests that cortical flows may determine the
500 initial position of the medial-axial AFBs, which assemble at predicted regions of high tension.
501 Observing breaks in the medial-axial AFBs and later the middle ridges of *nmy-1(RNAi)* adult-
502 stage alae further implicates this set of AFBs. During the L4-to-adult molt, these AFBs may
503 additionally resist excessive deformation of the apical membrane of the seam under the weight of
504 the growing alae. Manipulations that prevent the appropriate routing of forces would give rise to
505 uneven localized tension at the apical membrane, disordered blebs and subsequent alae
506 (mazes). In addition, insufficient resistance to axial stress would result in transverse breaks.
507 Similar specialized F-actin structures in the seam are not detected in immature seam cells or
508 during prior larval-to-larval molts.
509 CFBs beneath the apical membrane of hyp7 assemble while the seam widens and persist
510 through most of the molt. The CFBs were not sufficient to produce patterned alae, as CFBs were
511 detected in NMYII knockdowns associated with mazes. However, the formal possibility remains
512 that transient CFBs affect relaxation of the seam.
513 Knocking down core components of actomyosin networks had no appreciable effect on the
514 fundamental pattern of the annuli, suggesting that the CFBs in hyp7 are largely dispensable for
515 propagating the pattern of annuli from larval to adult-stage cuticles. In addition, variability in the
516 pattern of CFBs was not mirrored by abnormal patterning of the circumferential annuli. Instead,
517 transient CFBs detected in the lateral regions of hyp7 during the L4 to adult transition are
518 temporary elaborations of actin cables present in dorsal-lateral and ventral-lateral quadrants of
519 hyp7 and situated between the apical hemidesmosome-like plaques of fibrous organelles at all
520 times. In theory, these actin cables may be coupled to the apical membrane and thereby
521 components of the musculoskeletal system. One possibility is that these CFBs interact with the
522 actin-binding spectraplakin VAB-10B, which is similarly situated between the *Ce*HDs of late
523 embryos and larvae (Bosher et al., 2003).
524 Three aspects of alae morphogenesis bear similarity to embryonic elongation: large-scale
525 epidermal actin cytoskeleton rearrangements; the involvement of a temporary sheath capable of
526 propagating mechanical forces; and compaction of the body, albeit to very different extents.
527 Elongation is driven by forces generated by actomyosin contractility in the seam and distributed
528 through CFBs in the hypodermis as well as the sheath (Vuong-Brender et al., 2017a; Vuong-
529 Brender et al., 2017b). The CFBs present in the hypodermis of embryos are morphologically
530 similar to those we describe at the L4-to-adult transition. However, our results suggest that forces
531 generated by the longitudinal AFBs at the junctions between the seam and hyp7 route stress
532 through the sheath and not CFBs. The larval sheath also appears to be similar in composition
533 and function to its embryonic counterpart. For example, FBN-1 and NOAH-1 are components of
534 both (Kelley et al., 2015; Vuong-Brender et al., 2017b). However, the role of the embryonic sheath
535 in L1 alae morphogenesis has not been determined. Compaction is most striking in elongation,

536 when the embryo transforms from a ball of cells into a long, thin, tapered worm (Priess and Hirsh,
537 1986). In contrast, compaction during the molts has been reported (Uppaluri and Brangwynne,
538 2015), but seems temporary to accommodate enlargement of the cuticle. The transition from L2d
539 to dauer may present an exception, as radial constriction requires ZP-domain proteins called
540 cuticulins, some of which are found in dauer alae while others may localize to the L2d/dauer
541 sheath (Sapio et al., 2005).
542 These findings uncover a novel but likely conserved morphogenetic mechanism that links
543 mechanical networks driving apical constriction with matrix dynamics. Given that the key
544 intracellular and extracellular molecules are conserved between nematode and mammals, this
545 new system is likely relevant to mammalian physiology and pathology.
546
547 **MATERIALS AND METHODS**

548 **Strains and Molecular Biology**
549 *C. elegans* strains used in this study are listed in Table S1. Strains were maintained under
550 standard conditions and cultivated at 25ºC unless otherwise specified (Brenner, 1974). For
551 synchronization, gravid worms were bleached to isolate eggs, hatchlings arrested in starvation-
552 induced L1 diapause, and released from diapause by plating on NGM seeded with *E. coli* OP50-1.
553 Selected behaviors were scored to bin worms prior to mounting them on slides: locomotion and
554 feeding indicated non-molting worms; quiescence indicated molting worms (Cassada and
555 Russell, 1975); and idiosyncratic movements used to escape larval cuticles indicated ecdysis
556 (Singh and Sulston, 1978). The precise stages of L4 and adult worms were further determined
557 based on the shape of the gonad, vulva and lateral epidermis (Hubbard and Greenstein, 2005;
558 Mok et al., 2015; Sulston and Horvitz, 1977). Cuticle caps over the mouth were indicative of worms
559 undergoing molts (Monsalve et al., 2011). Strains with conditional alleles were propagated at
560 permissive temperature (15ºC) and cultivated at restrictive temperature (25ºC) following release
561 from starvation-induced L1 diapause. Bacterial-mediated RNA-interference (RNAi) was
562 performed as described (Fraser et al., 2000; Kamath and Ahringer, 2003; Timmons et al., 2001),
563 except that NGM (nematode growth medium) plates were supplemented with 8mM, rather than
564 1mM, isopropyl β-D-1-thiogalactopyranoside (IPTG). For attenuated RNAi treatments, animals
565 were washed off from control plates 14hrs after release from L1 diapause with 14ml M9, rotated
566 for 30 minutes in M9 to remove residual gut bacteria, and then transferred to experimental RNAi
567 plates. As a control, worms were fed the same *E. coli* HT115(DE3) transformed with pPD129.36.
568 Upon induction by IPTG, such bacteria produce short dsRNA molecules that does not match any
569 annotated gene of *C. elegans*.
570 Table S2 describes the oligonucleotides used in this study. Phusion High Fidelity Polymerase
571 (NEB) was used to amplify DNA for sequencing and cloning. Taq Polymerase (NEB) was used
572 for PCR-based genotyping. Gibson assembly (NEB) and standard cloning reactions were used to

573 construct fusion genes and corresponding plasmids. To create the *seam>rde-1+*
574 *elt-5p::rde-1::sl2-mcherry::unc-54* 3'-UTR fusion gene housed in pSK08, the promoter of *elt-5*,
575 which corresponds to nucleotides 1910072-1913471 of chromosome IV (GenBank: NC_003282);
576 the coding region of *rde-1*, which corresponds to nucleotides 9988043-9991614 of chromosome
577 V (GenBank: NC_003283); coding sequence for *mCherry* (GenBank: KT175701), *sl2* (GenBank:
578 LK928133); and the *unc-54* 3'-UTR cassette from pPD95.75 were combined. To construct the
579 *hyp-7>rde-1+ dpy-7p::rde-1::sl2::nls-gfp::unc-54* 3'-UTR fusion gene housed in pSK38, the
580 minimal promoter of *dpy-7*, which corresponds to nucleotides 7537789-7537869 and 7537914-
581 7538219 of chromosome X (GenBank: NC_003284); the coding region of *rde-1*; *SL2*; and the *nls-*
582 *gfp::unc-54* 3'-UTR cassette from pPD95.73 were united. To construct the
583 *dpy-7p::utrnch::dsred::unc-54* 3'-UTR fusion gene housed in pSK26, the promoter of *dpy-7* (as
584 above); the coding sequence for the first CH domain (residues 1-261) of human Utrophin
585 (GenBank: LX69086); the coding sequence for *dsRed* (GenBank: HQ418395); the *unc-54* 3'-UTR
586 cassette from pPD95.81; and the pUC57 backbone were combined. To construct the
587 *elt-5p::utrnch::gfp::unc-54* 3'-UTR fusion gene housed in pSK34, the promoter of *elt-5*; the
588 sequence encoding UTRNCH; and the *gfp::unc-54* 3'-UTR cassette and backbone from
589 pPD95.81 were united. All variants of plasmids pPD95 were gifts from Andy Fire.
590 Towards the production of a full-length *fbn-1::mCherry* fusion gene, genomic DNA spanning
591 3.6kb of upstream sequence and exons 1-14 of *fbn-1k* (Genbank: JQ990128); cDNA spanning
592 exons 14-22 isolated from pMH281 (Maxwell Heiman, Harvard Medical School); and genomic
593 DNA spanning exons 21-25 and the 3'-UTR of *fbn-1k* were combined in plasmid pSK27. The latter
594 fragment was modified by insertion of an in-frame *NotI-mCherry-NotI* cassette between the
595 codons for H2418 and V2419 of *fbn-1k*. *mCherry* was isolated from KP1272 (Joshua Kaplan,
596 HMS). A 7.4 kb region of genomic DNA spanning the entire promoter and exons 1-2 of *fbn-1* was
597 amplified separately. pSK27 and the purified PCR product were co-injected at an equimolar ratio,
598 allowing for homologous recombination *in vivo* (see below). The genomic DNA present in the full
599 length (fl) *fbn-1::mCherry* fusion gene corresponds to nucleotides 7619229-7641053 of
600 chromosome III (GenBank: LK928224). To construct the *noah-1::sfGFP::noah-1* translational
601 fusion gene housed in pCM05, regulatory and coding regions of *noah-1* were amplified from
602 genomic DNA (nucleotides 5874389-5883950 of chromosome I, GenBank: LK927608) and
603 cloned into a NotI-filled derivate of pCR-Blunt II-TOPO (Invitrogen). A *NotI-sfgfp-NotI* cassette
604 was inserted in-frame between the codons for P624 and V625 of *noah-1a* (Genbank:
605 NM_170870). The corresponding NotI site was created using a Q5 mutagenesis kit (Invitrogen).
606 Superfolder (sf) GFP was isolated from pCW11 (Max Heiman, Harvard University).
607 All extrachromosomal arrays were generated by microinjection of young adults with mixtures
608 containing a total of 100ng/µl DNA. To generate *aaaEx37*, pSK08 (5ng/µl); *ttx-3::gfp* (40ng/µl);
609 and pRS316 (55ng/µl) were co-injected into JK537 *rde-1(ne219)*. To generate *aaaEx162*, pSK38

610 (5ng/µl); *ttx-3::dsred* (40ng/µl); and pRS316 were co-injected into JK537. To generate *aaaEx108*,
611 pSK26 (0.5ng/µl); *ttx-3::gfp*; and pRS316 were co-injected into N2. To generate *aaaEx117*,
612 pSK34 (5ng/µl); *ttx-3::gfp*; and pRS316 were co-injected into N2. Optimal plasmid concentrations
613 used to generate tandem *utrnch* arrays were empirically determined by titration. UTRNCH signals
614 were readily detected in the resulting transgenic animals, while phenotypes associated with high
615 levels of UTRN were not observed. To generate *aaaEx78[fl-fbn-1::mCherry::fbn-1],* pSK27 (2.5
616 ng/µl); the above-mentioned PCR product (1.15 ng/µl); *ttx-3p::gfp*; and pRS316 were co-injected
617 into N2. To generate *aaaEx167*, pCM05 (1ng/µl); *ttx-3::dsred*; and pRS316 were co-injected into
618 ARF379. Resulting transgenic lines were out-crossed to N2 to remove *aaaIs12*.
619 Extrachromosomal arrays were integrated into the genome by UV irradiation at 450 kJ using an
620 FB-UVXL-1000 (Fisher Scientific). Strains with newly-integrated arrays were back-crossed to
621 JK537 or N2 4 to 6 times prior to further analyses.
622 To knockdown *actin* by bacterial-mediated RNAi, we used the clone for *act-2* present in the
623 Ahringer library (Kamath and Ahringer, 2003). Towards knocking-down *nmy-1* (Genbank:
624 LK927643), 1121bp of genomic DNA from exon 10 was cloned into pPD129.36, the standard
625 expression vector for dsRNAs. For *zoo-1* (GenBank: NM_001026515), cDNA spanning exons 1-7
626 was cloned into pPD129.36, as previously described (Lockwood et al., 2008). For *noah-1*
627 (GenBank: LK927608), 1024bp from exon 6 was cloned into pPD129.36. Each of the resulting
628 plasmids (pSK43, pSK44 and pCM13) was verified by Sanger sequencing and used to transform
629 *E. coli* strain HT115(DE3).
630
631 **DiI Staining of Cuticles**
632 DiI staining to visualize cuticle structures was performed basically as described (Schultz and
633 Gumienny, 2012), except that glass pipettes were used to transfer samples in lieu of Triton X-
634 100. Briefly, approximately 600 adult worms were incubated in 400µl of 30 µg/mL DiI (Sigma) in
635 M9 for 3 hours, shaking at 350rpm. Worms were then washed 1X in M9 buffer, re-suspended in
636 100µl of M9, and dispensed to a 6cm NGM plate seeded with *E. coli* OP50-1. To remove excess
637 unbound dye, worms were allowed to crawl on the plate for 30min prior to imaging.
638
639 **Microscopy and Image Analyses**
640 Worms were anesthetized with sodium azide (2.5%) in M9 buffer and mounted on 2% agarose
641 pads. A Zeiss Axioplan microscope with an attached Hamamatsu Orca ER CCD camera was
642 used for compound microscopy. Images were acquired and analyzed using the software package
643 Volocity 6.3 (PerkinElmer). A Zeiss LSM 5 PASCAL microscope controlled by ZEN 9.0 software
644 was typically used for confocal microscopy. A Zeiss LSM880 laser scanning confocal microscope
645 was used as specified. Measurements were made using Volocity 6.3 (PerkinElmer), ImageJ
646 (Version 1.48v, NIH), and Fiji (Schindelin et al., 2012). To determine furrow spacing from images

647 of DiI-stained cuticles, we used the Find Peaks BAR script in Fiji. This tool identified local minima
648 from linescan plots, also made in Fiji. Three to four linescans were made per image. Seam width
649 was measured in Fiji as the distance between AJM-1::mCHERRY-marked junctions. Six
650 measurements were made per image. Volocity was used to measure fluorescence intensity in
651 manually-selected, similarly-sized regions along the margins of hyp7. Four ROIs were assayed
652 per worm. The ImageJ plugin FibrilTool was used to measure anisotropy (Boudaoud et al., 2014).
653 For each worm assayed, 6 values were obtained by subdividing the lateral region of hyp7 into 3
654 dorsal and 3 ventral ROIs, each approximately 400μm^2.
655 For transmission electron microscopy (TEM), synchronized wild-type (N2) animals were
656 collected, washed once in 8% ethanol and M9, and washed 3 times in PBS over a period of 30
657 mins. Specimens were suspended in 2.5% glutaraldehyde, 1% paraformaldehyde and 0.1M
658 sucrose in PBS; incubated for 2 hours on ice; and incubated for 16 hours at 4°C. Samples were
659 washed, post-fixed in 1% OsO4, and dehydrated by serial immersion in graded ethanol solutions.
660 Samples were then passed through propylene oxide, embedded in serial steps using mixtures of
661 propylene oxide and Epon 812, and cured at 60°C for 48 hrs. An RMC MTX ultramicrotome was
662 used to cut 60 nm-thick sections, which were stained with uranyl acetate and lead citrate. Sections
663 were observed using a 100CX JEOL electron microscope.
664
665 **Statistical Analyses and Image Presentation**
666 GraphPad Prism 6 and Microsoft Excel 15.21 were used for statistical analyses. To perform
667 statistical analyses in Figures 2B, 3B, and 8D, the mazes, gaps, and other phenotypical
668 categories were combined so that and outcomes were classified as abnormal versus superficially
669 normal. All micrographs were prepared for publication using Adobe Photoshop v13.0 and Adobe
670 Illustrator v16.0.
671
672 **ACKNOWLEDGEMENTS**

673 Some strains used in this study were provided by the *Caenorhabditis* Genetics Center, which is
674 funded by the NIH Office of Research Infrastructure Programs (P40 OD010440). We are grateful
675 to Margot Quinlan, Alvaro Sagasti, and Larry Zipursky for helpful discussions. We thank Hannah
676 Maul-Newby and Dominic Williams for valuable technical assistance. We also thank Margot
677 Quinlan, John Kim, Eric Miska, and David Sherwood for sharing reagents. A Ruth L. Kirschstein
678 National Research Service Award (GM007185 to SK), UCLA Dissertation Year Fellowship (SK),
679 and a National Science Foundation Award (IOS 1258218 to ARF) supported this research.

680 **FIGURE LEGENDS**

681 **Figure 1. Revised model for progression of the L4/A molt and formation of the alae.**
682 Illustrations of *C. elegans* body sections depict changes in the epidermis, cortical actin networks
683 therein, and overlying matrices. These drawings encapsulate both existing knowledge and new
684 findings described in this report.

685

686 **Figure 2. Knockdown of epidermal actin or NMYII results in maze-like deformities on adult**
687 **cuticles. A)** Representative DIC micrographs show the lateral surfaces of young adults of the
688 indicated genotypes. The ">" symbols refer to promoter fusions, as described in the methods and
689 Table S1. Brackets demarcate regions above seam syncytia. Yellow and black dashes label
690 presumptive longitudinal ridges (alae) and adjacent valleys, respectively. Arrows and arrowheads
691 point to mazes and minor deformities in alae. Asterisk labels a gap. **B)** Quantitation of alae
692 defects. Values are weighted averages from 2 independent trials. P<0.001 for all pairwise
693 comparisons between control and *actin(RNAi)* or *nmy-1(RNAi)* cohorts; Fisher's exact test with
694 Bonferroni's correction for multiple comparisons. **C)** Confocal fluorescence micrographs show Dil-
695 stained cuticles of young adults. Arrows to a single annulus and similar structures; arrowheads
696 point to malformed alae. The mean furrow spacing (±SD) for each genotype is listed underneath
697 corresponding images. Schematic depicts the normal pattern of Dil-staining. Scale bars = 5µm.
698 Strains used were ARF330, ARF408, N2, WM179 and WM180.

699

700 **Figure 3. Knockdown of α-catenin and ZO-1 results in mazes on adult cuticles. A)** As
701 described for Fig. 2, DIC micrographs show segments of lateral cuticles. **B)** Quantitation of alae
702 defects. Values are weighted averages 2 two independent trials. ****P<0.0002, $^{n.s.}$P>0.99,
703 Fisher's exact test with Bonferroni's correction for multiple comparisons. **C)** Confocal fluorescence
704 micrographs show Dil-labeled dorsal- or ventral-lateral surfaces of adult cuticles. Arrows point to
705 an annulus and a superficially similar band. Mfs= mean furrow spacing of corresponding
706 genotype, ±SD. Scale bars = 5µm. Strains N2 and PE97 were imaged.

707

708 **Figure 4. Actin dynamics linked to pulsatile constriction of the seam cortex. A)** Diagrams
709 depict the seam cells and syncytia of juvenile and mature *C. elegans*. Images in B and C generally
710 correspond to the indicated region of interest (ROI). **B)** Representative confocal fluorescence
711 projections show signals from seam>UTRNCH::GFP (false colored magenta) and/or the AJ
712 marker AJM-1::mCHERRY (false colored green). Yellow lines label longitudinal actin bundles at
713 the dorsal and ventral margins. Dashes label medial-axial actin bundles within seam syncytia (s).
714 Arrow points to cortical actin mesh. Chevrons point to F-actin spikes orthogonal to seam/hyp7
715 margins. **C)** Quantitation of seam width measured as distance between AJM-1::mCHERRY-
716 marked junctions. Lines and error bars indicate the mean and standard deviation. ****P≤0.0001,

717 ***P≤0.001, $^{n.s.}$P>0.05; Ordinary one-way ANOVA with Tukey's method for multiple comparisons.
718 Scale bar = 5μm. Strain imaged was ARF404.
719
720 **Figure 5. Contractility is required to maintain seam shape.** Confocal fluorescence projections
721 show F-actin and AJ signals in worms NMYII knockdowns transiting the L4/Adult molt.
722 Arrowheads point to small breaks in medial-axial AFBs. Images were acquired using a Zeiss
723 LSM880 with Airyscan processing. Scale bar = 5μm. Strains imaged were ARF404 and ARF410.
724
725 **Figure 6. Cortical actin dynamics in lateral regions of hyp7. A)** Representative confocal
726 fluorescence projections show F-actin labeled by hyp>UTRNCH::dsRED across the larval-to-
727 adult transition. Arrowheads point to F-actin at margins adjoining the syncytial seam; chevrons
728 point to segments with little or no detectable signal. Arrows point to circumferential actin filament
729 bundles (CFBs). Circles mark puncta. Digitally-brightened ROI (2X exposure) shows CFBs in the
730 region of hyp7 overlying body wall muscles. These micrographs were selected from images of
731 over 130 precisely staged specimens. **B)** Quantitation of F-actin signals at the margins of hyp7.
732 Lines and error bars indicate the mean and standard deviation. ****P≤0.0001, **P≤0.01,
733 $^{n.s.}$P>0.05; Ordinary one-way ANOVA with Tukey's method for multiple comparisons. **C)**
734 Quantitation of the anisotropy of F-actin signals in laterals region of hyp7. Values for signal
735 intensity and anisotropy represent 4 and 6 ROIs per worm, respectively; N=3-7 per stage and
736 condition. **D)** Confocal fluorescence projections show signals from hyp7>UTRNCH::dsRED in
737 molting animals of the indicated genotypes. **E)** Quantitation (as in C) of corresponding F-actin
738 signals at hyp7 margins. **F)** Quantitation of the anisotropy of F-actin signals (as in E). Scale bars
739 = 10μm. Strains imaged were ARF385 and ARF388.
740
741 **Figure 7. Changes in tissue ultrastructure coupled to morphogenesis of the alae. A)** TEM
742 micrographs show transverse sections through the seam and hyp7 syncytia of early and mid-L4
743 wild-type larvae (25,000X). Brackets demarcate the width of the seam surface; aj = apical
744 junctions. Arrowheads outline the seam syncytium. The singular arrow points to the provisional
745 sheath situated above cellular protrusions and beneath the L4 cuticle. Adapted with permission
746 from Singh and Sulston (1978) (Singh and Sulston, 1978). **B)** Comparable TEM micrographs
747 across the L4/A molt show invagination and expansion of the seam cortex during deposition of
748 the alae. Brackets demarcate effete larval cuticles; arrowheads point to emergent adult cuticles;
749 arrows point to presumptive remnants of the sheath. Chevrons point to secretory granules in the
750 seam. **C)** Transverse TEM section shows the alae and lateral epidermis of a young adult at the
751 same magnification. Scale bar = 500nm. The complementary illustration depicts the epidermal
752 syncytia and mature alae of an adult worm from the same perspective.
753

754 **Figure 8. Actin is required to pattern sheath components, which then pattern the alae.**
755 **A)** Representative confocal fluorescence projections show FL-FBN-1::mCHERRY detected in the
756 sheaths of control and attenuated *actin(RNAi)* animals molting from L4 to the adult stage. Vertical
757 arrows mark fluorescent annular bands within the sheath. Brackets demarcate the underlying
758 seam syncytia. Dashed rectangles indicate ROIs digitally enlarged in adjacent panels. In control,
759 ROI corresponds to a maximum intensity projection omitting surface slices. Yellow dashes label
760 fluorescent longitudinal cables detected on the lateral surface of the control specimen; black
761 dashes label the same sites on the corresponding DIC micrograph. Arrowheads point to
762 fluorescent maze-like fibrils detected on the lateral surface of the attenuated *actin(RNAi)*
763 specimen and similar substructures on the emergent cuticle. Fluorescent signals were false-
764 colored yellow to make the overlays. Images were acquired using a Zeiss LSM880 with
765 Airyscan processing. **B)** As described, NOAH-1::GFP primarily localizes to the sheath. These
766 representative confocal projections show residual signals detected on the surface of newly-
767 emerged control and attenuated *actin(RNAi)* adults, essentially as in A. **C)** Representative DIC
768 micrographs show the lateral surfaces of young adults. Black and yellow dots label longitudinal
769 ridges (alae) and adjacent valleys on the control specimen. Arrow points to a maze on the *noah-*
770 *1(RNAi)* animal. **D)** Quantitation of alae defects. As previously described, values are the weighted
771 average of 2 independent trials. ****P<0.0001; Fisher's exact test. Scale bars = 5μm. Strains used
772 were ARF379, ARF415, and N2.
773
774 **Figure 9. Synopsis of key findings and model for morphogenesis of the adult-stage alae.**
775 **A)** Graphical representation of the lateral surface of the seam and hyp7 syncytia across the larval-
776 to-adult transition. Cortical actin networks are depicted in red. Inward facing arrows (2) represent
777 apical constriction of the seam syncytium driven by net compressive forces. Outward facing
778 arrows (3) represent gradual expansion of the seam controlled by the dynamic exchange of
779 mechanical forces among epidermal syncytia and the molting sheath. **B)** Graphical representation
780 of a transverse cross-section through the lateral epidermis and overlying matrices at the apex of
781 constriction (A2) and subsequent relaxation (A4) of the seam cortex. The related model for
782 patterning the alae is fully described in the discussion.

783 **SUPPLEMENTAL MATERIALS**

784 **Supplemental Figure 1. Cortical actin dynamics in seam cells prior to homotypic fusion.**
785 Representative confocal fluorescence projections (lateral view) show signals from
786 seam>UTRNCH::GFP and the AJ marker AJM-1::mCHERRY detected across the L3-to-L4
787 transition. UTRNCH::GFP is false colored magenta; AJM-1::mCHERRY, green in merged images.
788 Bracket demarcates the space between two posterior daughter cells previously occupied by an
789 anterior daughter cell that fused with hyp7, and bridged by UTRNCH::GFP signal. Arrows points
790 to concentrated UTRNCH::GFP signal at the junction between daughter cells. s=seam; a=anterior
791 and p=posterior daughter cell. Strain imaged was ARF404. Scale bar = 5μm.
792

793 **Supplemental Figure 2. CFBs in thin regions of hyp7 interdigitate with hemidesmosomes**
794 **and some extend over the lateral epidermis while animals molt. A)** Confocal fluorescence
795 projections show signals from hyp7>UTRNCH::dsRED (magenta in merge) and MUP-4::GFP
796 6hrs into the L4 stage. MUP-4 is a nematode-specific ECM receptor associated with apical *Ce*HDs
797 and corresponding fibrous organelles. The dashed line distinguishes the thick, lateral region of
798 hyp7 overlying the pseudocoelom (lh7) and the thin region overlying body wall muscles (mh7).
799 Arrows points to one example of a continuous CFB that spans both regions and contacts the
800 seam/hyp7 margin. s= seam. **B)** Merged projections of the same 2 signals show intercalated
801 stripes of F-actin and MUP-4 across the L4-to-adult transition. **C)** Confocal fluorescence
802 micrographs show F-actin labeled by UTRNCH::dsRED and *Ce.*HDs marked by VAB-10A::GFP
803 detected at the surface of mh7 in a young adult. The corresponding linescan shows non-
804 overlapping peaks. Images were acquired using a Zeiss LSM 880 with linear unmixing of dsRED
805 and GFP signals. Strains imaged were ARF412 and ARF407. Scale bars = 5μm.
806

807 **Supplemental Figure 3. Cortical actin and apical ECM dynamics across the L2d-to-dauer**
808 **transition. A)** Confocal fluorescence projections show F-actin labeled by UTRNCH::GFP in the
809 non-fused seam cells of *daf-2(e1370)* larvae. Dashed lines and arrowheads label longitudinal and
810 transverse actin bundles, respectively, detected early in the L2d to dauer molt. Chevrons point to
811 spikes of F-actin orthogonal to the margins of very narrow cells. **B)** Confocal fluorescence
812 projection shows FL-FBN-1::mCHERRY detected on the surface of a molting *daf-2(e1370)*
813 animal. Yellow dashed lines label distinct longitudinal stripes of FL-FBN-1::mCHERRY, numbered
814 pairwise at right, reflecting bilateral symmetry. Bracket demarcates the presumed underlying
815 seam width prior to constriction. Arrow points to a circumferential band of FL-FBN-1::mCHERRY.
816 (Bottom) Trace of dauer alae in published transverse TEM micrographs {Cassada, 1975 #100}
817 shows characteristic ridges and valleys. **C)** For comparison, this overexposed fluorescence
818 micrograph shows that signals from FL-FBN-1::mCHERRY were not detected on the surface of a

819 dauer larva. The bracket on the corresponding DIC micrograph demarcates the dauer alae.
820 Strains imaged were ARF416, ARF417, and ARF321. Scale bars = 5μm.
821
822 **Supplemental Table 1:** *C. elegans* strains used in this study.
823
824 **Supplemental Table 2:** Oligonucleotides used in this study.
825

REFERENCES

Bercher, M., J. Wahl, B.E. Vogel, C. Lu, E.M. Hedgecock, D.H. Hall, and J.D. Plenefisch. 2001. mua-3, a gene required for mechanical tissue integrity in Caenorhabditis elegans, encodes a novel transmembrane protein of epithelial attachment complexes. *The Journal of cell biology*. 154:415-426.

Borghi, N., M. Sorokina, O.G. Shcherbakova, W.I. Weis, B.L. Pruitt, W.J. Nelson, and A.R. Dunn. 2012. E-cadherin is under constitutive actomyosin-generated tension that is increased at cell-cell contacts upon externally applied stretch. *Proceedings of the National Academy of Sciences of the United States of America*. 109:12568-12573.

Bosher, J.M., B.S. Hahn, R. Legouis, S. Sookhareea, R.M. Weimer, A. Gansmuller, A.D. Chisholm, A.M. Rose, J.L. Bessereau, and M. Labouesse. 2003. The Caenorhabditis elegans vab-10 spectraplakin isoforms protect the epidermis against internal and external forces. *The Journal of cell biology*. 161:757-768.

Boudaoud, A., A. Burian, D. Borowska-Wykret, M. Uyttewaal, R. Wrzalik, D. Kwiatkowska, and O. Hamant. 2014. FibrilTool, an ImageJ plug-in to quantify fibrillar structures in raw microscopy images. *Nature protocols*. 9:457-463.

Braidotti, P., P.G. Nuciforo, J. Mollenhauer, A. Poustka, C. Pellegrini, A. Moro, G. Bulfamante, G. Coggi, S. Bosari, and G.G. Pietra. 2004. DMBT1 expression is down-regulated in breast cancer. *BMC Cancer*. 4:46.

Brenner, S. 1974. The genetics of Caenorhabditis elegans. *Genetics*. 77:71-94.

Burkel, B.M., G. von Dassow, and W.M. Bement. 2007. Versatile fluorescent probes for actin filaments based on the actin-binding domain of utrophin. *Cell motility and the cytoskeleton*. 64:822-832.

Cao, J., M. Ehling, S. Marz, J. Seebach, K. Tarbashevich, T. Sixta, M.E. Pitulescu, A.C. Werner, B. Flach, E. Montanez, E. Raz, R.H. Adams, and H. Schnittler. 2017. Polarized actin and VE-cadherin dynamics regulate junctional remodelling and cell migration during sprouting angiogenesis. *Nat Commun*. 8:2210.

Cassada, R.C., and R.L. Russell. 1975. The dauerlarva, a post-embryonic developmental variant of the nematode Caenorhabditis elegans. *Dev Biol*. 46:326-342.

Costa, M., B.W. Draper, and J.R. Priess. 1997. The role of actin filaments in patterning the Caenorhabditis elegans cuticle. *Dev Biol*. 184:373-384.

Costa, M., W. Raich, C. Agbunag, B. Leung, J. Hardin, and J.R. Priess. 1998. A putative catenin-cadherin system mediates morphogenesis of the Caenorhabditis elegans embryo. *The Journal of cell biology*. 141:297-308.

Cox, E.A., and J. Hardin. 2004. Sticky worms: adhesion complexes in C. elegans. *Journal of cell science*. 117:1885-1897.

Devuyst, O., E. Olinger, and L. Rampoldi. 2017. Uromodulin: from physiology to rare and complex kidney disorders. *Nat Rev Nephrol*. 13:525-544.

Essmann, C.L., M. Elmi, M. Shaw, G.M. Anand, V.M. Pawar, and M.A. Srinivasan. 2017. In-vivo high resolution AFM topographic imaging of Caenorhabditis elegans reveals previously unreported surface structures of cuticle mutants. *Nanomedicine*. 13:183-189.

Fabritius, H., C. Sachs, D. Raabe, S. Nikolov, M. Friák, and J. Neugebauer. 2011. Chitin in the Exoskeletons of Arthropoda: From Ancient Design to Novel Materials Science. *In* Chitin: Formation and Diagenesis. N.S. Gupta, editor. Springer Netherlands, Dordrecht. 35-60.

Frand, A.R., S. Russel, and G. Ruvkun. 2005. Functional genomic analysis of C. elegans molting. *PLoS Biol*. 3:e312.

Fraser, A.G., R.S. Kamath, P. Zipperlen, M. Martinez-Campos, M. Sohrmann, and J. Ahringer. 2000. Functional genomic analysis of C. elegans chromosome I by systematic RNA interference. *Nature*. 408:325-330.

Gupta, R., H. Birch, K. Rapacki, S. Brunak, and J.E. Hansen. 1999. O-GLYCBASE version 4.0: a revised database of O-glycosylated proteins. *Nucleic Acids Res*. 27:370-372.

Hannezo, E., B. Dong, P. Recho, J.F. Joanny, and S. Hayashi. 2015. Cortical instability drives periodic supracellular actin pattern formation in epithelial tubes. *Proceedings of the National Academy of Sciences of the United States of America*. 112:8620-8625.

880 Hayashi, K., A. Makino, and D. Kakoi. 2018. Remodeling of arterial wall: Response to changes in
881 both blood flow and blood pressure. *J Mech Behav Biomed Mater*. 77:475-484.
882 Heer, N.C., and A.C. Martin. 2017. Tension, contraction and tissue morphogenesis. *Development*.
883 144:4249-4260.
884 Hong, L., T. Elbl, J. Ward, C. Franzini-Armstrong, K.K. Rybicka, B.K. Gatewood, D.L. Baillie, and
885 E.A. Bucher. 2001. MUP-4 is a novel transmembrane protein with functions in epithelial cell
886 adhesion in Caenorhabditis elegans. *The Journal of cell biology*. 154:403-414.
887 Hu, P.J. 2007. Dauer. *WormBook : the online review of C. elegans biology*:1-19.
888 Hubbard, E.J., and D. Greenstein. 2005. Introduction to the germ line. *WormBook : the online*
889 *review of C. elegans biology*:1-4.
890 Iruela-Arispe, M.L., and G.J. Beitel. 2013. Tubulogenesis. *Development*. 140:2851-2855.
891 Jenkin, P.M., and H.E. Hinton. 1966. Apolysis in arthropod moulting cycles. *Nature*. 211:871.
892 Johnstone, I.L., Y. Shafi, and J.D. Barry. 1992. Molecular analysis of mutations in the
893 Caenorhabditis elegans collagen gene dpy-7. *Embo J*. 11:3857-3863.
894 Jonckheere, N., N. Skrypek, and I. Van Seuningen. 2010. Mucins and pancreatic cancer. *Cancers*
895 *(Basel)*. 2:1794-1812.
896 Kamath, R.S., and J. Ahringer. 2003. Genome-wide RNAi screening in Caenorhabditis elegans.
897 *Methods*. 30:313-321.
898 Kang, H., I. Bang, K.S. Jin, B. Lee, J. Lee, X. Shao, J.A. Heier, A.V. Kwiatkowski, W.J. Nelson, J.
899 Hardin, W.I. Weis, and H.J. Choi. 2017. Structural and functional characterization of
900 Caenorhabditis elegans alpha-catenin reveals constitutive binding to beta-catenin and F-actin.
901 *The Journal of biological chemistry*. 292:7077-7086.
902 Katz, S., H. Maul-Newby, T. Chong, V. Meli, and A. Frand. 2015. FBN-1 is an apical matrix protein
903 essential for the integrity of epithelial organs under mechanical stress during larval
904 development., International Worm Meeting.
905 Kelley, M., J. Yochem, M. Krieg, A. Calixto, M.G. Heiman, A. Kuzmanov, V. Meli, M. Chalfie, M.B.
906 Goodman, S. Shaham, A. Frand, and D.S. Fay. 2015. FBN-1, a fibrillin-related protein, is
907 required for resistance of the epidermis to mechanical deformation during C. elegans
908 embryogenesis. *Elife*. 4.
909 Kim, H.Y., V.D. Varner, and C.M. Nelson. 2013. Apical constriction initiates new bud formation
910 during monopodial branching of the embryonic chicken lung. *Development*. 140:3146-3155.
911 Knight, C.G., M.N. Patel, R.B. Azevedo, and A.M. Leroi. 2002. A novel mode of ecdysozoan
912 growth in Caenorhabditis elegans. *Evol Dev*. 4:16-27.
913 Koh, K., and J.H. Rothman. 2001. ELT-5 and ELT-6 are required continuously to regulate
914 epidermal seam cell differentiation and cell fusion in C. elegans. *Development*. 128:2867-
915 2880.
916 Koppen, M., J.S. Simske, P.A. Sims, B.L. Firestein, D.H. Hall, A.D. Radice, C. Rongo, and J.D.
917 Hardin. 2001. Cooperative regulation of AJM-1 controls junctional integrity in Caenorhabditis
918 elegans epithelia. *Nature cell biology*. 3:983-991.
919 Lampugnani, M.G. 2010. Endothelial adherens junctions and the actin cytoskeleton: an 'infinity
920 net'? *J Biol*. 9:16.
921 Legan, P.K., V.A. Lukashkina, R.J. Goodyear, A.N. Lukashkin, K. Verhoeven, G. Van Camp, I.J.
922 Russell, and G.P. Richardson. 2005. A deafness mutation isolates a second role for the
923 tectorial membrane in hearing. *Nat Neurosci*. 8:1035-1042.
924 Locke, M., and P. Huie. 1979. Apolysis and the turnover of plasma membrane plaques during
925 cuticle formation in an insect. *Tissue Cell*. 11:277-291.
926 Lockwood, C., R. Zaidel-Bar, and J. Hardin. 2008. The C. elegans zonula occludens ortholog
927 cooperates with the cadherin complex to recruit actin during morphogenesis. *Curr Biol*.
928 18:1333-1337.
929 Loveless, T., and J. Hardin. 2012. Cadherin complexity: recent insights into cadherin superfamily
930 function in C. elegans. *Curr Opin Cell Biol*. 24:695-701.
931 MacQueen, A.J., J.J. Baggett, N. Perumov, R.A. Bauer, T. Januszewski, L. Schriefer, and J.A.
932 Waddle. 2005. ACT-5 is an essential Caenorhabditis elegans actin required for intestinal
933 microvilli formation. *Molecular biology of the cell*. 16:3247-3259.

934 Maiden, S.L., N. Harrison, J. Keegan, B. Cain, A.M. Lynch, J. Pettitt, and J. Hardin. 2013. Specific
935 conserved C-terminal amino acids of Caenorhabditis elegans HMP-1/alpha-catenin modulate
936 F-actin binding independently of vinculin. *The Journal of biological chemistry*. 288:5694-5706.
937 Martin, A.C., M. Gelbart, R. Fernandez-Gonzalez, M. Kaschube, and E.F. Wieschaus. 2010.
938 Integration of contractile forces during tissue invagination. *The Journal of cell biology*.
939 188:735-749.
940 Martin, A.C., and B. Goldstein. 2014. Apical constriction: themes and variations on a cellular
941 mechanism driving morphogenesis. *Development*. 141:1987-1998.
942 Mason, F.M., M. Tworoger, and A.C. Martin. 2013. Apical domain polarization localizes actin-
943 myosin activity to drive ratchet-like apical constriction. *Nature cell biology*. 15:926-936.
944 Masuya, H., K. Shimizu, H. Sezutsu, Y. Sakuraba, J. Nagano, A. Shimizu, N. Fujimoto, A. Kawai,
945 I. Miura, H. Kaneda, K. Kobayashi, J. Ishijima, T. Maeda, Y. Gondo, T. Noda, S. Wakana, and
946 T. Shiroishi. 2005. Enamelin (Enam) is essential for amelogenesis: ENU-induced mouse
947 mutants as models for different clinical subtypes of human amelogenesis imperfecta (AI). *Hum*
948 *Mol Genet*. 14:575-583.
949 McMahon, L., R. Legouis, J.L. Vonesch, and M. Labouesse. 2001. Assembly of C. elegans apical
950 junctions involves positioning and compaction by LET-413 and protein aggregation by the
951 MAGUK protein DLG-1. *Journal of cell science*. 114:2265-2277.
952 Mok, D.Z., P.W. Sternberg, and T. Inoue. 2015. Morphologically defined sub-stages of C. elegans
953 vulval development in the fourth larval stage. *BMC Dev Biol*. 15:26.
954 Monsalve, G.C., C. Van Buskirk, and A.R. Frand. 2011. LIN-42/PERIOD controls cyclical and
955 developmental progression of C. elegans molts. *Curr Biol*. 21:2033-2045.
956 Moores, C.A., and J. Kendrick-Jones. 2000. Biochemical characterisation of the actin-binding
957 properties of utrophin. *Cell motility and the cytoskeleton*. 46:116-128.
958 Morrissey, M.A., D.P. Keeley, E.J. Hagedorn, S.T. McClatchey, Q. Chi, D.H. Hall, and D.R.
959 Sherwood. 2014. B-LINK: a hemicentin, plakin, and integrin-dependent adhesion system that
960 links tissues by connecting adjacent basement membranes. *Developmental cell*. 31:319-331.
961 Muller, U., and P.G. Barr-Gillespie. 2015. New treatment options for hearing loss. *Nat Rev Drug*
962 *Discov*. 14:346-365.
963 Nelson, C.M. 2016. On Buckling Morphogenesis. *J Biomech Eng*. 138:021005.
964 Page, A.P., and I.L. Johnstone. 2007. The cuticle. *WormBook : the online review of C. elegans*
965 *biology*:1-15.
966 Pasti, G., and M. Labouesse. 2014. Epithelial junctions, cytoskeleton, and polarity. *WormBook :*
967 *the online review of C. elegans biology*:1-35.
968 Pettitt, J., E.A. Cox, I.D. Broadbent, A. Flett, and J. Hardin. 2003. The Caenorhabditis elegans
969 p120 catenin homologue, JAC-1, modulates cadherin-catenin function during epidermal
970 morphogenesis. *The Journal of cell biology*. 162:15-22.
971 Piekny, A.J., J.L. Johnson, G.D. Cham, and P.E. Mains. 2003. The Caenorhabditis elegans
972 nonmuscle myosin genes nmy-1 and nmy-2 function as redundant components of the let-
973 502/Rho-binding kinase and mel-11/myosin phosphatase pathway during embryonic
974 morphogenesis. *Development*. 130:5695-5704.
975 Podbilewicz, B., and J.G. White. 1994. Cell fusions in the developing epithelial of C. elegans. *Dev*
976 *Biol*. 161:408-424.
977 Priess, J.R., and D.I. Hirsh. 1986. Caenorhabditis elegans morphogenesis: the role of the
978 cytoskeleton in elongation of the embryo. *Dev Biol*. 117:156-173.
979 Qadota, H., M. Inoue, T. Hikita, M. Koppen, J.D. Hardin, M. Amano, D.G. Moerman, and K.
980 Kaibuchi. 2007. Establishment of a tissue-specific RNAi system in C. elegans. *Gene*. 400:166-
981 173.
982 Sapio, M.R., M.A. Hilliard, M. Cermola, R. Favre, and P. Bazzicalupo. 2005. The Zona Pellucida
983 domain containing proteins, CUT-1, CUT-3 and CUT-5, play essential roles in the
984 development of the larval alae in Caenorhabditis elegans. *Dev Biol*. 282:231-245.
985 Sarov, M., J.I. Murray, K. Schanze, A. Pozniakovski, W. Niu, K. Angermann, S. Hasse, M.
986 Rupprecht, E. Vinis, M. Tinney, E. Preston, A. Zinke, S. Enst, T. Teichgraber, J. Janette, K.
987 Reis, S. Janosch, S. Schloissnig, R.K. Ejsmont, C. Slightam, X. Xu, S.K. Kim, V. Reinke, A.F.

988 Stewart, M. Snyder, R.H. Waterston, and A.A. Hyman. 2012. A genome-scale resource for in
989 vivo tag-based protein function exploration in C. elegans. *Cell*. 150:855-866.
990 Schindelin, J., I. Arganda-Carreras, E. Frise, V. Kaynig, M. Longair, T. Pietzsch, S. Preibisch, C.
991 Rueden, S. Saalfeld, B. Schmid, J.Y. Tinevez, D.J. White, V. Hartenstein, K. Eliceiri, P.
992 Tomancak, and A. Cardona. 2012. Fiji: an open-source platform for biological-image analysis.
993 *Nature methods*. 9:676-682.
994 Schultz, R.D., and T.L. Gumienny. 2012. Visualization of Caenorhabditis elegans cuticular
995 structures using the lipophilic vital dye DiI. *J Vis Exp*:e3362.
996 Shih, P.J., I.J. Wang, W.F. Cai, and J.Y. Yen. 2017. Biomechanical Simulation of Stress
997 Concentration and Intraocular Pressure in Corneas Subjected to Myopic Refractive Surgical
998 Procedures. *Sci Rep*. 7:13906.
999 Singh, R.N., and J.E. Sulston. 1978. Some Observations on Molting in Caenorhabditis-Elegans.
1000 *Nematologica*. 24:63-&.
1001 Steiner, F.A., K.L. Okihara, S.W. Hoogstrate, T. Sijen, and R.F. Ketting. 2009. RDE-1 slicer
1002 activity is required only for passenger-strand cleavage during RNAi in Caenorhabditis
1003 elegans. *Nat Struct Mol Biol*. 16:207-211.
1004 Sulston, J.E., and H.R. Horvitz. 1977. Post-embryonic cell lineages of the nematode,
1005 Caenorhabditis elegans. *Dev Biol*. 56:110-156.
1006 Timmons, L., D.L. Court, and A. Fire. 2001. Ingestion of bacterially expressed dsRNAs can
1007 produce specific and potent genetic interference in Caenorhabditis elegans. *Gene*. 263:103-
1008 112.
1009 Truman, J.W. 1992. The eclosion hormone system of insects. *Prog Brain Res*. 92:361-374.
1010 Uppaluri, S., and C.P. Brangwynne. 2015. A size threshold governs Caenorhabditis elegans
1011 developmental progression. *Proc Biol Sci*. 282:20151283.
1012 Vasquez, C.G., M. Tworoger, and A.C. Martin. 2014. Dynamic myosin phosphorylation regulates
1013 contractile pulses and tissue integrity during epithelial morphogenesis. *The Journal of cell*
1014 *biology*. 206:435-450.
1015 Vuong-Brender, T.T., M. Ben Amar, J. Pontabry, and M. Labouesse. 2017a. The interplay of
1016 stiffness and force anisotropies drives embryo elongation. *Elife*. 6.
1017 Vuong-Brender, T.T.K., S.K. Suman, and M. Labouesse. 2017b. The apical ECM preserves
1018 embryonic integrity and distributes mechanical stress during morphogenesis. *Development*.
1019 Willis, J.H., E. Munro, R. Lyczak, and B. Bowerman. 2006. Conditional dominant mutations in the
1020 Caenorhabditis elegans gene act-2 identify cytoplasmic and muscle roles for a redundant
1021 actin isoform. *Molecular biology of the cell*. 17:1051-1064.
1022 Wu, S.K., and A.S. Yap. 2013. Patterns in space: coordinating adhesion and actomyosin
1023 contractility at E-cadherin junctions. *Cell Commun Adhes*. 20:201-212.
1024

Figure 1

Katz et al. (2018)

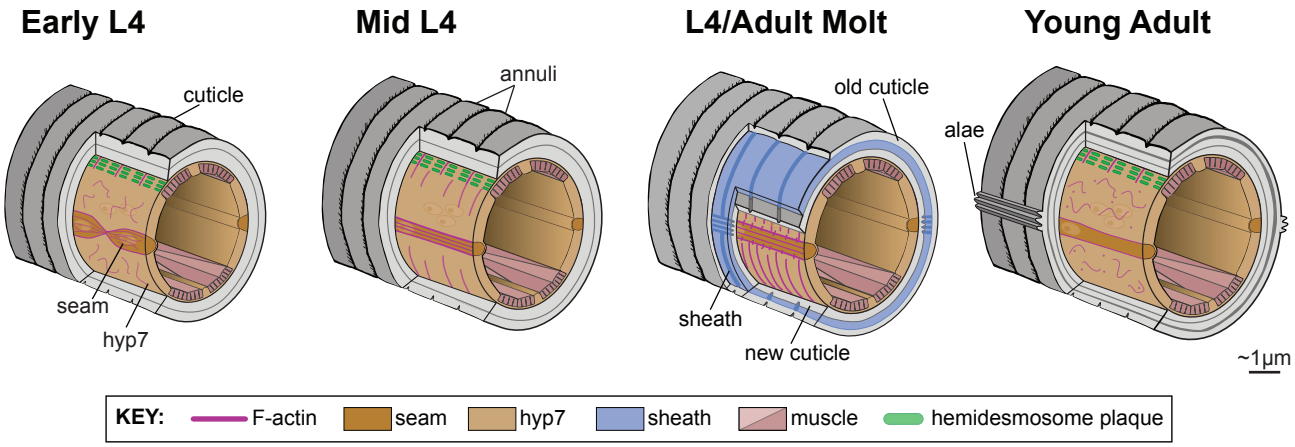

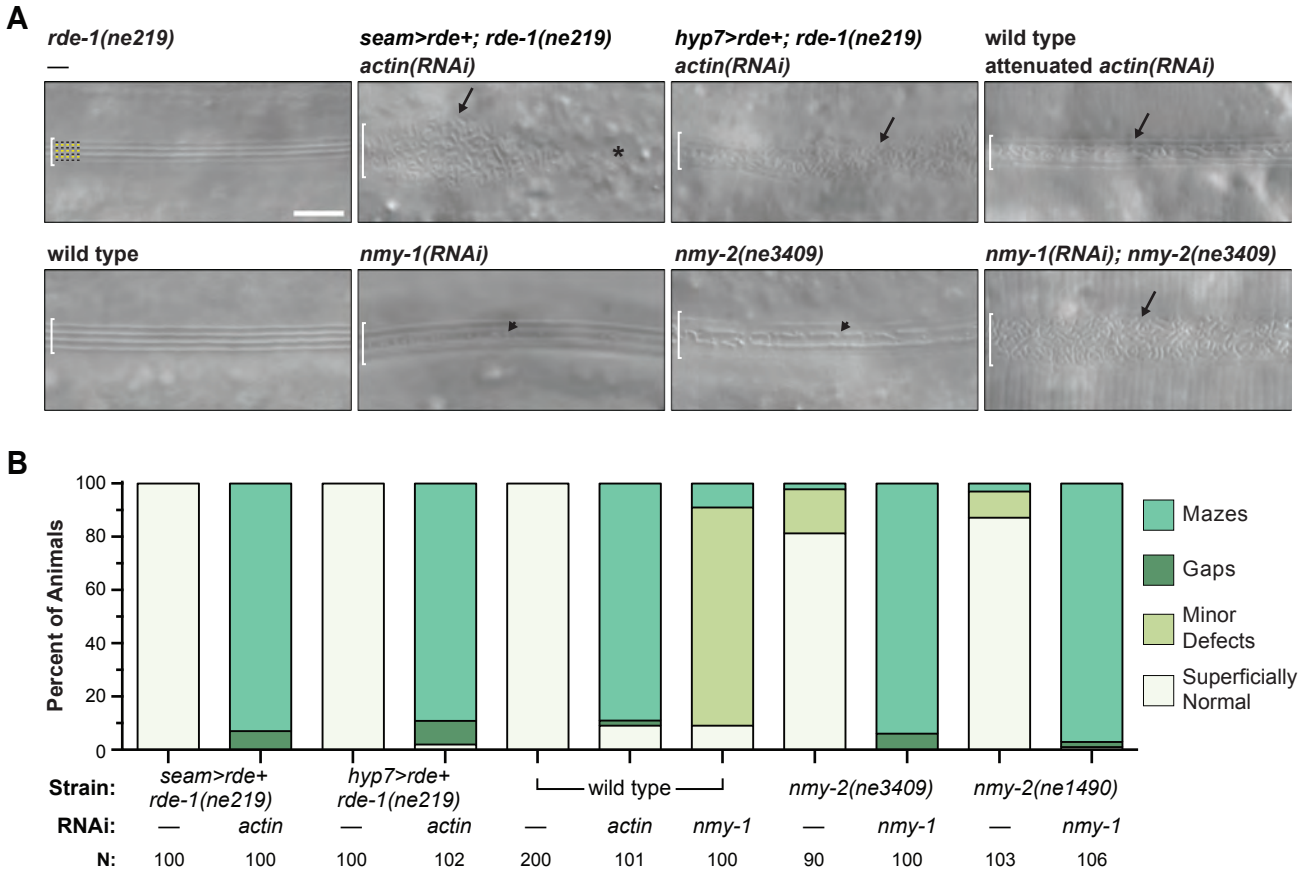
A
rde-1(ne219)
—
seam>rde+; rde-1(ne219)
actin(RNAi)
hyp7>rde+; rde-1(ne219)
actin(RNAi)
wild type
attenuated actin(RNAi)
wild type
nmy-1(RNAi)
nmy-2(ne3409)
nmy-1(RNAi); nmy-2(ne3409)
B
Percent of Animals
100
80
60
40
20
0
Mazes
Gaps
Minor Defects
Superficially Normal
Strain:
seam>rde+ rde-1(ne219)
hyp7>rde+ rde-1(ne219)
wild type
nmy-2(ne3409)
nmy-2(ne1490)
RNAi:
— actin — actin — actin nmy-1 — nmy-1 — nmy-1
N:
100 100 100 102 200 101 100 90 100 103 106

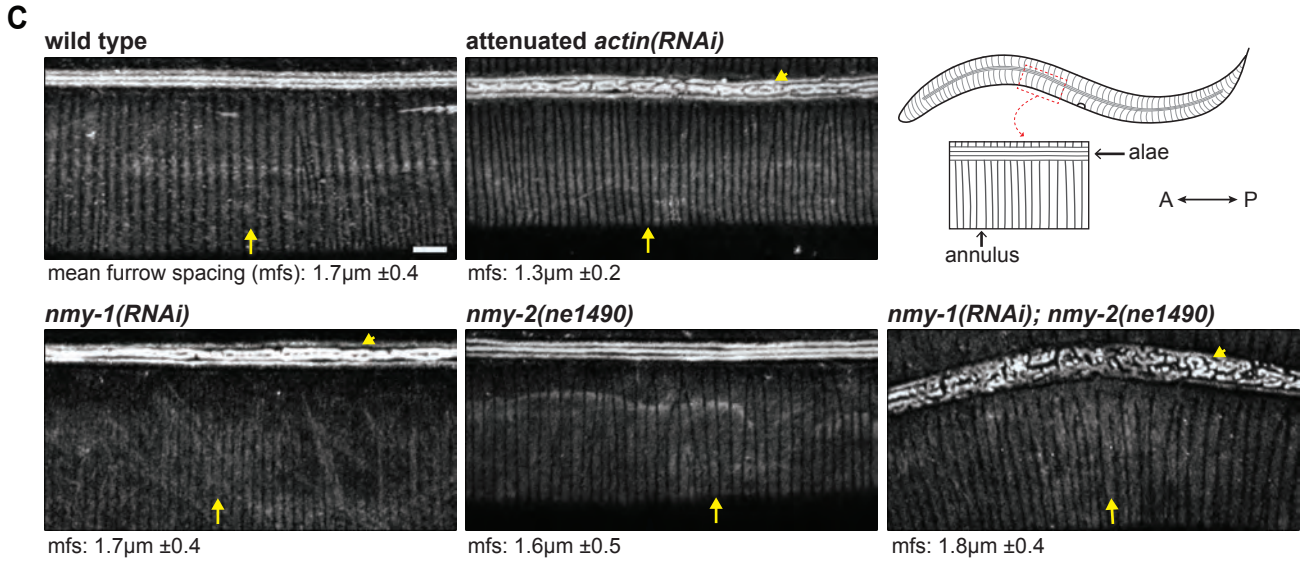
C
wild type
mean furrow spacing (mfs): 1.7μm ±0.4
attenuated actin(RNAi)
mfs: 1.3μm ±0.2
alae
A P
annulus
nmy-1(RNAi)
mfs: 1.7μm ±0.4
nmy-2(ne1490)
mfs: 1.6μm ±0.5
nmy-1(RNAi); nmy-2(ne1490)
mfs: 1.8μm ±0.4

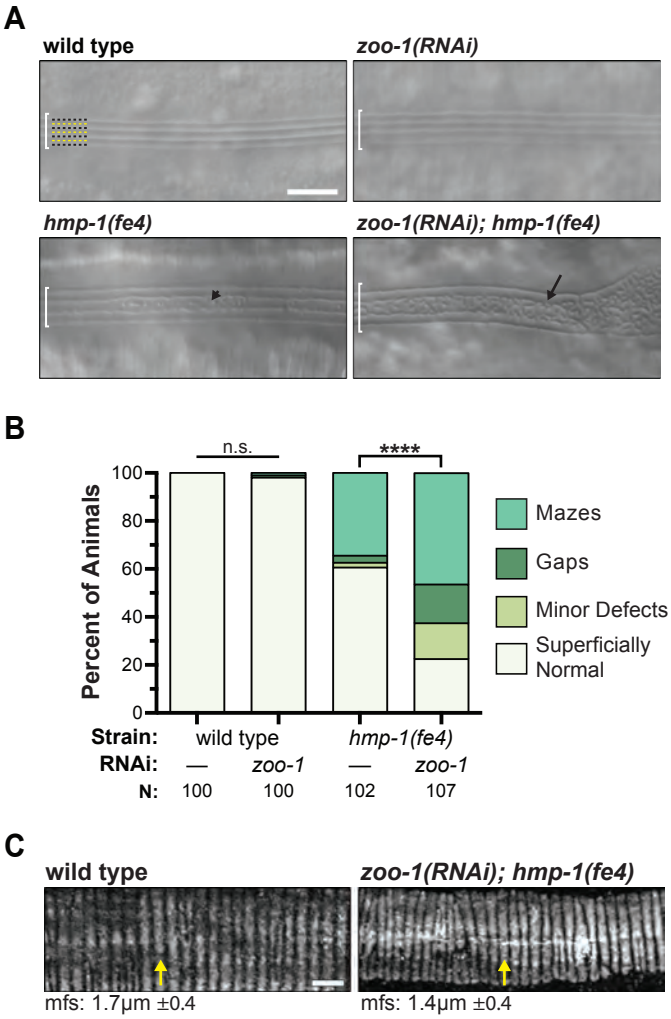
A
wild type
zoo-1(RNAi)
hmp-1(fe4)
zoo-1(RNAi); hmp-1(fe4)
B
n.s.
****
Percent of Animals
100
80
60
40
20
0
Mazes
Gaps
Minor Defects
Superficially Normal
Strain: wild type hmp-1(fe4)
RNAi: — zoo-1 — zoo-1
N: 100 100 102 107
C
wild type
zoo-1(RNAi); hmp-1(fe4)
mfs: 1.7µm ±0.4
mfs: 1.4µm ±0.4

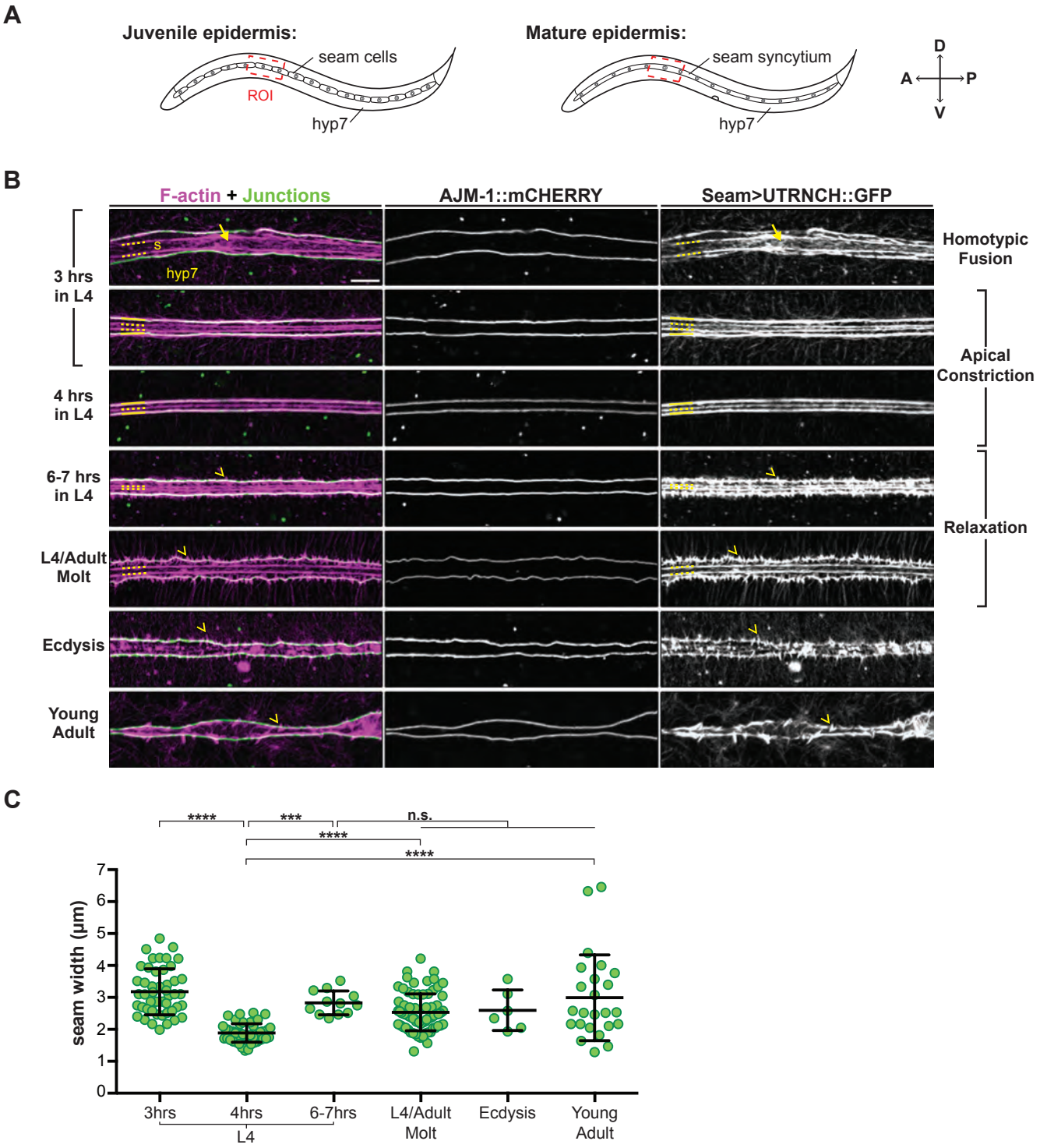
A
Juvenile epidermis:
seam cells
ROI
hyp7
Mature epidermis:
seam syncytium
hyp7
D
A
P
V
B
F-actin + Junctions
AJM-1::mCHERRY
Seam>UTRNCH::GFP
3 hrs in L4
4 hrs in L4
6-7 hrs in L4
L4/Adult Molt
Ecdysis
Young Adult
s
hyp7
Homotypic Fusion
Apical Constriction
Relaxation
C
seam width (µm)
0
1
2
3
4
5
6
7
****
***
n.s.
****
****
3hrs
4hrs
6-7hrs
L4/Adult Molt
Ecdysis
Young Adult
L4

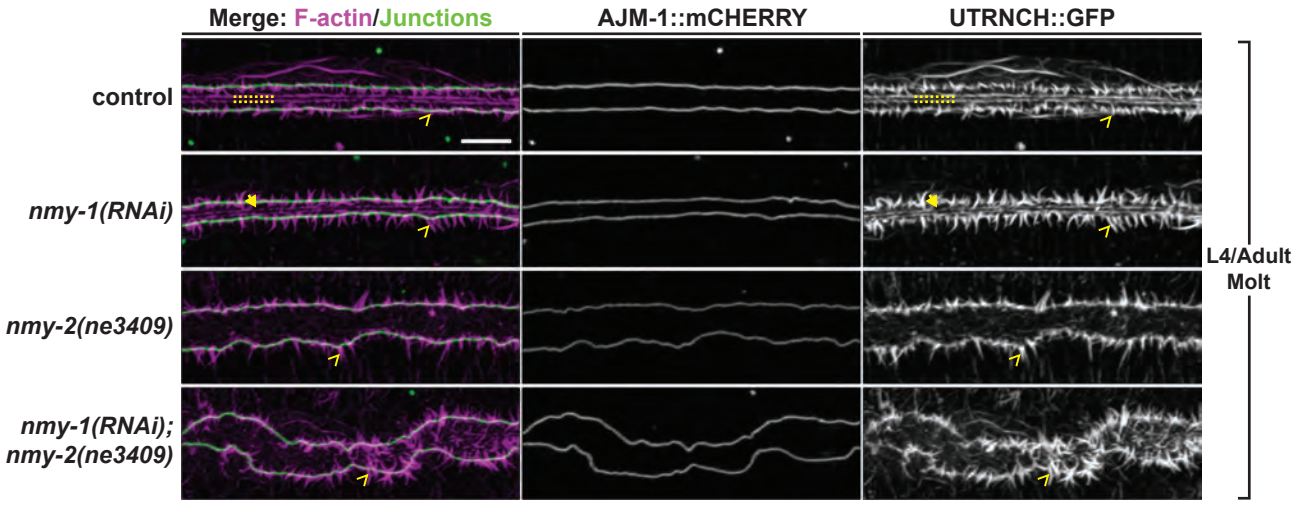
Merge: F-actin/Junctions
AJM-1::mCHERRY
UTRNCH::GFP
control
nmy-1(RNAi)
nmy-2(ne3409)
nmy-1(RNAi);
nmy-2(ne3409)
L4/Adult
Molt

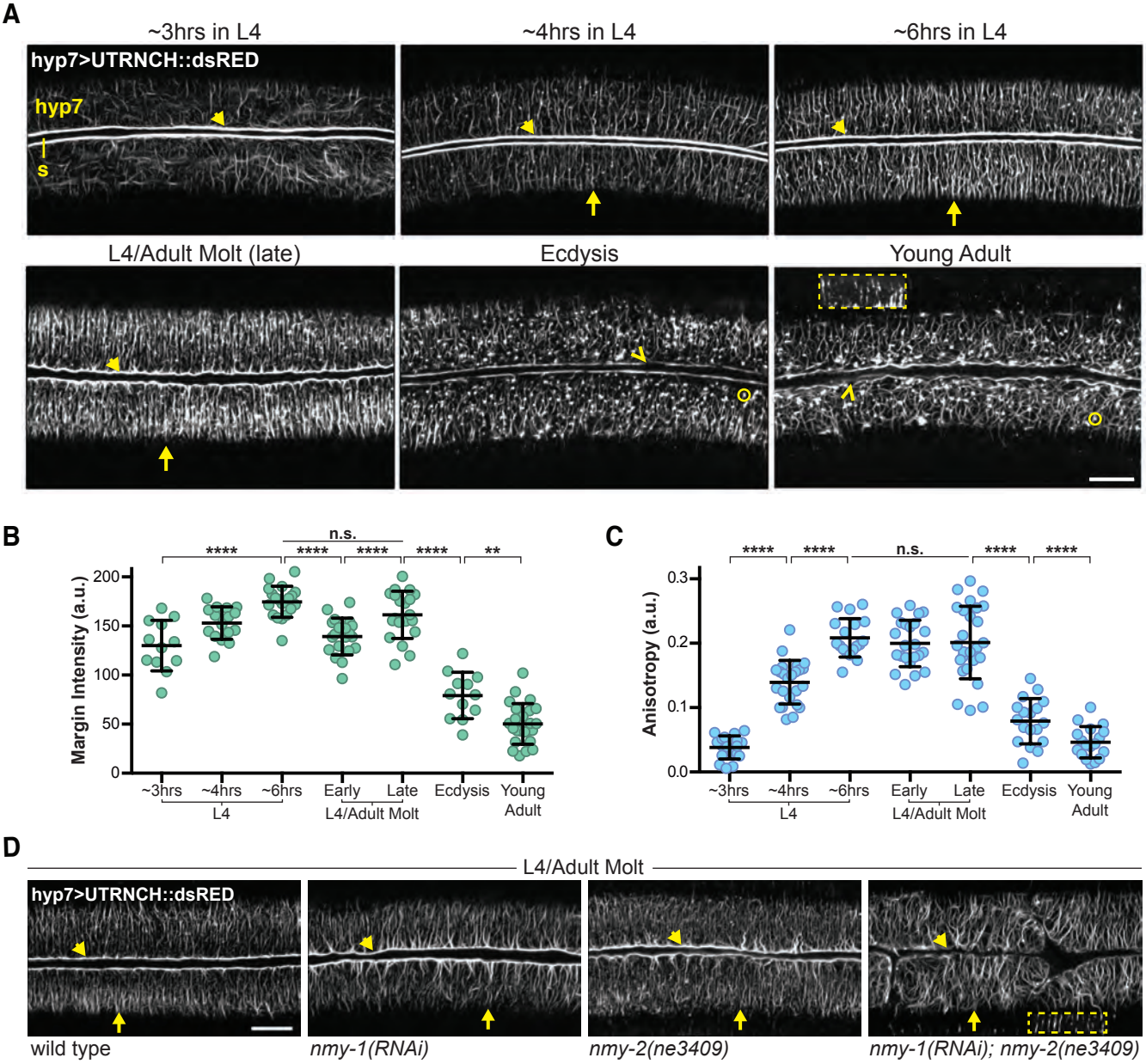
A
~3hrs in L4
~4hrs in L4
~6hrs in L4
hyp7>UTRNCH::dsRED
hyp7
s
L4/Adult Molt (late)
Ecdysis
Young Adult
B
Margin Intensity (a.u.)
n.s.
****
**
~3hrs
~4hrs
~6hrs
Early
Late
Ecdysis
Young Adult
L4
L4/Adult Molt
C
Anisotropy (a.u.)
n.s.
****
D
L4/Adult Molt
hyp7>UTRNCH::dsRED
wild type
nmy-1(RNAi)
nmy-2(ne3409)
nmy-1(RNAi); nmy-2(ne3409)
E
Margin Intensity (a.u.)
Genotype: wild type nmy-2(ne3409)
RNAi: — nmy-1 — nmy-1
F
Anisotropy (a.u.)
n.s.
Genotype: wild type nmy-2(ne3409)
RNAi: — nmy-1 — nmy-1
c.o.v.: 21% 26% 15% 47%

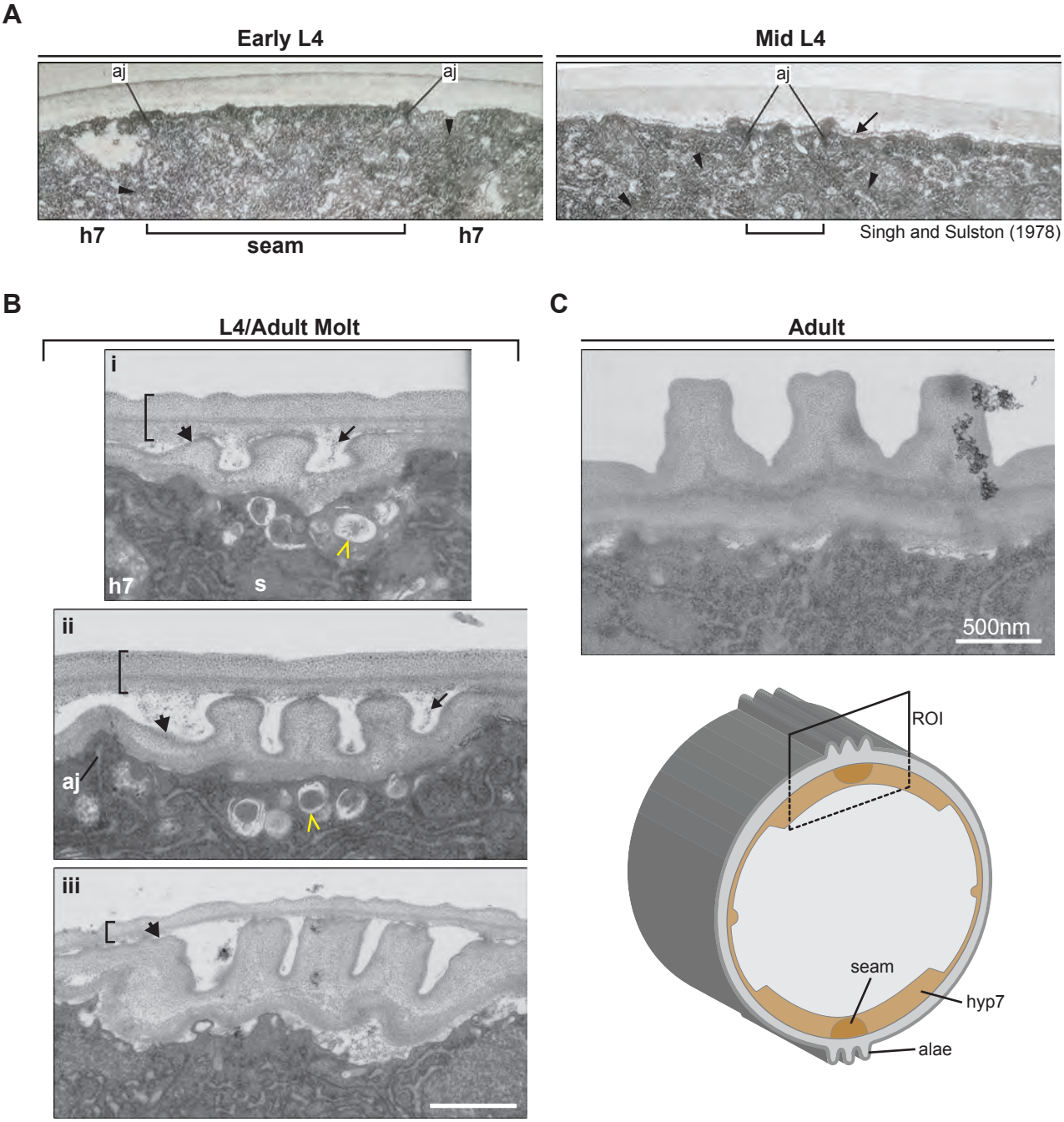
A
Early L4
aj
aj
h7
seam
h7
Mid L4
aj
Singh and Sulston (1978)
B
L4/Adult Molt
i
h7
s
ii
aj
iii
C
Adult
500nm
ROI
seam
hyp7
alae

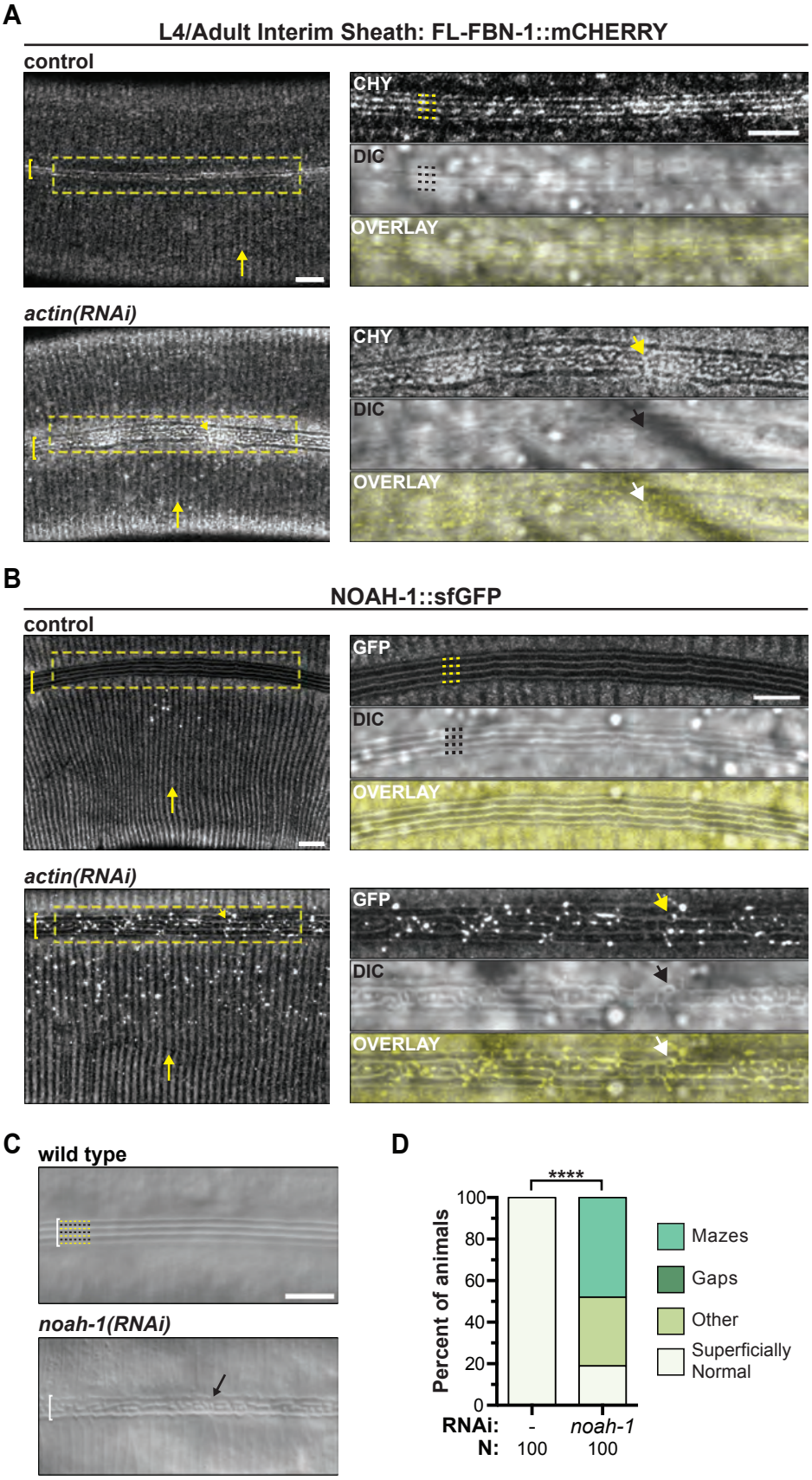
A
L4/Adult Interim Sheath: FL-FBN-1::mCHERRY
control
CHY
DIC
OVERLAY
actin(RNAi)
CHY
DIC
OVERLAY
B
NOAH-1::sfGFP
control
GFP
DIC
OVERLAY
actin(RNAi)
GFP
DIC
OVERLAY
C
wild type
noah-1(RNAi)
D
****
Percent of animals
100
80
60
40
20
0
RNAi: - noah-1
N: 100 100
Mazes
Gaps
Other
Superficially Normal

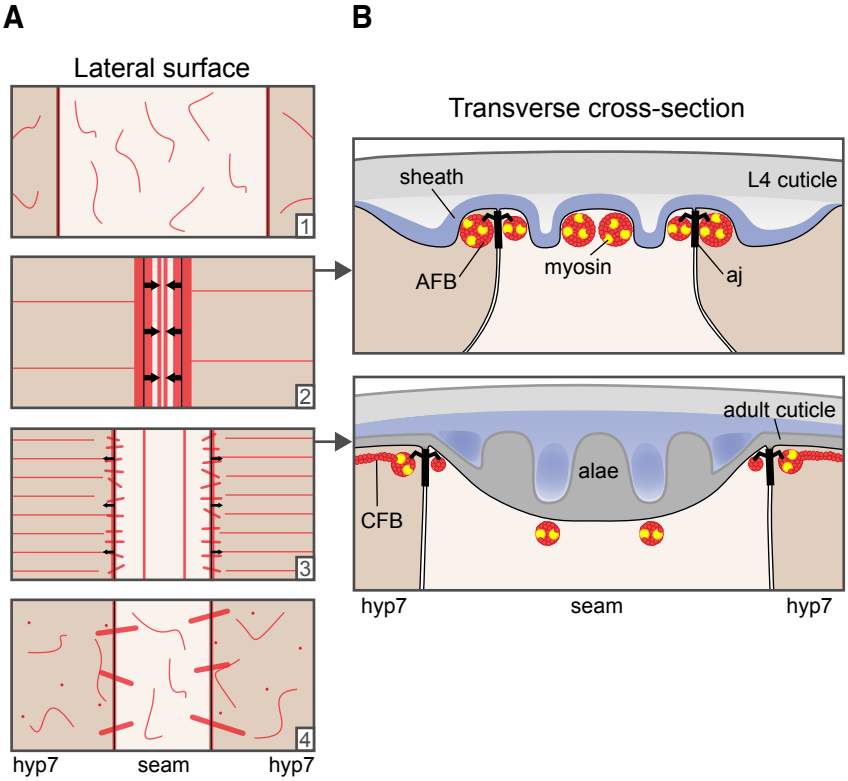
A
B
Lateral surface
Transverse cross-section
1
2
3
4
hyp7
seam
hyp7
sheath
L4 cuticle
AFB
myosin
aj
adult cuticle
alae
CFB
hyp7
seam
hyp7